nature biotechnology

Article

https://doi.org/10.1038/s41587-023-01957-8

Killing tumor-associated bacteria with a liposomal antibiotic generates neoantigens that induce anti-tumor immune responses

Received: 4 May 2022

Accepted: 18 August 2023

Published online: 25 September 2023

Check for updates

Menglin Wang[1], Benoit Rousseau[2], Kunyu Qiu[1], Guannan Huang[3,4,5], Yu Zhang[1], Hang Su[6], Christine Le Bihan-Benjamin[7], Ines Khati[7], Oliver Artz[2], Michael B. Foote[2], Yung-Yi Cheng[8], Kuo-Hsiung Lee[8,9], Michael Z. Miao[10,11], Yue Sun[12], Philippe-Jean Bousquet[13], Marc Hilmi[14,15], Elise Dumas[16,17,18], Anne-Sophie Hamy[16,19], Fabien Reyal[16,20,21], Lin Lin[22], Paul M. Armistead[22,23], Wantong Song[24,25], Ava Vargason[1], Janelle C. Arthur[3,5,26], Yun Liu[1], Jianfeng Guo[1], Xuefei Zhou[1], Juliane Nguyen[1], Yongqun He[27,28,29], Jenny P.-Y. Ting[3,4,5,30], Aaron C. Anselmo[1] & Leaf Huang[1] ✉

Increasing evidence implicates the tumor microbiota as a factor that can influence cancer progression. In patients with colorectal cancer (CRC), we found that pre-resection antibiotics targeting anaerobic bacteria substantially improved disease-free survival by 25.5%. For mouse studies, we designed an antibiotic silver-tinidazole complex encapsulated in liposomes (LipoAgTNZ) to eliminate tumor-associated bacteria in the primary tumor and liver metastases without causing gut microbiome dysbiosis. Mouse CRC models colonized by tumor-promoting bacteria (*Fusobacterium nucleatum* spp.) or probiotics (*Escherichia coli* Nissle spp.) responded to LipoAgTNZ therapy, which enabled more than 70% long-term survival in two *F. nucleatum*-infected CRC models. The antibiotic treatment generated microbial neoantigens that elicited anti-tumor $CD8^+$ T cells. Heterologous and homologous bacterial epitopes contributed to the immunogenicity, priming T cells to recognize both infected and uninfected tumors. Our strategy targets tumor-associated bacteria to elicit anti-tumoral immunity, paving the way for microbiome–immunotherapy interventions.

Establishing immune responses against cancer-derived epitopes has become the mainstay of cancer immunotherapy[1]. Unleashing T cell immunity to elicit anti-tumor immune responses has led to important clinical advances against cancer, including checkpoint inhibitors, cancer vaccines and chimeric antigen receptor T cell (CAR-T) therapies[2]. Failures in achieving immunotherapy efficacy in colorectal cancer (CRC) have been attributed to both a low mutation load, resulting in the lack of mutation-derived neoantigens, and the immunosuppressive environment of the tumor. Tumors with low mutational burden pose greater challenges for personalized neoantigen vaccines—for example, in patients with microsatellite stable (MSS) CRC tumors. MSS CRC is typically resistant to immune checkpoint blockade, and innovative immunomodulating strategies are needed[3]. Recent studies have suggested that intratumoral bacteria are intracellularly present in both cancer and immune cells within the tumor microenvironment[4], which may provide an alternative source of neoepitopes for cancer immunotherapy. We hypothesize that killing the intracellular bacteria in the tumor will expose microbial epitopes and yield alternative sources of cancer-associated neoantigens.

A full list of affiliations appears at the end of the paper. ✉e-mail: leafh@email.unc.edu

Preclinical studies have shown that T cell immunity elicited by bacteria cross-react with major histocompatibility complex class I (MHC-I)-restricted antigens from cancer cells, suggesting that microbe-specific T cells contribute to anti-tumor immune responses[5,6]. A commensal Bacteroides species peptide mimic drove the progression of spontaneous autoimmune myocarditis depending on cardiac myosin-specific TH_{17} cells[7]. The microbiota elicits microbe-specific T cell responses that are speculated to escape from self-tolerance mechanisms. We hypothesize that homologous epitopes shared by both the bacteria and the host contribute to anti-tumor immunity.

Nanotechnology is a promising tool for the intracellular delivery of small molecules to the tumor site. Drug-loaded nanoparticles can specifically abolish the colonization of intracellular bacteria in the tumor[8]. In the present study, we tested a strategy by delivering liposomes loaded with a silver-tinidazole complex (LipoAgTNZ) by remote loading technology to bacteria-infected orthotopic CRC tumors in mice. We show here that eliminating bacteria from CRC tumors via liposomal delivery of antibiotics targeting anaerobic bacteria unleashed anti-tumor CD8 T cells. We analyzed the heterologous and homologous epitopes based on genome-wide alignment between the host and the colonizing bacteria. In an oncogenic *Fusobacterium nucleatum*-infected model, T cells responded to both *F. nucleatum* and host-shared epitopes. The killing of tumor-associated bacteria improved cancer therapy outcomes by exposing microbial epitopes.

Results

Antibiotics targeting anaerobes improved cancer survival

Microbial cells outnumber host cells nine-to-one in the human distal gut[9], which impart both beneficial and detrimental influences on host physiology[10]. Broad-spectrum antibiotic treatments compromise microbiome diversity and impair the efficacy of cancer immunotherapy[11,12]; therefore, an important therapeutic opportunity remains through the selective targeting of oncogenic bacteria that are associated with cancer malignancies—for example, gastric (*Helicobacter pylori*) and colorectal (*F. nucleatum* and *Bacteroides fragilis*) cancer[13,14]. Nitroimidazole and lincomycin are antibiotic classes approved to treat infections associated with anaerobic bacteria. We started our approach by investigating a nationwide pharmaco-epidemiologic database of patients with CRC to determine if resected patients with CRC exposed to these antibiotic classes had improved disease-free survival (DFS) compared to patients receiving other antibiotics or not receiving any antibiotics (Fig. 1a). Between 2012 and 2014, among 36,105 patients who had curative-intent resection of a colorectal tumor, a total of 4,413 patients with CRC, comprising 12% of the cohort, received antibiotic treatment of the nitroimidazole or lincomycin classes within 6 months before resection to 12 months after resection (Supplementary Fig. 1a). To limit time-dependent biases, the exposure to antibiotics was assessed as a time-dependent variable (Supplementary Fig. 1b). To obtain the specific effect of the group of antibiotics targeting *F. nucleatum*, multivariate Cox models were performed on the group of patients who did not receive antibiotics other than one included in this class.

As we previously reported a prognostic interaction between antibiotic intake and chemotherapy exposure[15], we focused our analysis on patients who did not received any cytotoxic treatment. The hazard ratio (HR) was lower for antibiotics targeting anaerobes than without antibiotics administration among patients with CRC. This protective effect occurred in the patients who received antibiotics before resection of the tumor but not after resection (Fig. 1b). After resection, the protective effect of antibiotics targeting anaerobes did not occur, which suggests a specific role of these antibiotics when the tumor has not yet been removed. Taking antibiotics targeting anaerobes when the tumor is a target lesion reduced the risk of recurrence or death by 25.5% (HR = 0.745, 95% confidence interval (CI) 0.57–0.98, two-sided $P = 0.037$) (Supplementary Fig. 1c). Colorectal tumors have direct accessibility to gut microbiota and oral availability to antibiotics; therefore, to assess the specific role of tumor primary, we studied an independent cohort of patients with breast cancer ($n = 94{,}484$, with 688 patients exposed to nitroimidazole or lincomycin). This protective effect was not found in patients with breast cancer in a multivariate model using the same methodology and adjusted for breast-cancer-relevant prognosis factors (Supplementary Fig. 2a), suggesting that this protective role is specific to CRC and its microbiota. Comparing patients receiving antibiotics targeting anaerobes with patients receiving other antibiotics, we also confirmed that the DFS was improved for antibiotics targeting anaerobes before resection of CRC compared to other antibiotics (P(log rank) = 0.019; Fig. 1c). Again, this effect was not observed for patients with breast cancer (Supplementary Fig. 2b). The results strengthen the hypothesis that specific antibiotics have the potential to reduce the risk of recurrence of CRC with an effect that may be as important as chemotherapy, which usually reduces the risk of recurrence by 32% or death by 26% after resection in combination with adjuvant treatments[16]. Although the microbiota status of the patients is not known in the database, the encouraging clinical results for specific classes of antibiotics covering anaerobic bacteria have prompted us to establish a well-defined, bacteria-infected murine model for detailed study.

Bacteria invaded tumor cells in response to low oxygen level

Gram-negative and anaerobic bacteria, *F. nucleatum*, are prevalent in human CRC as well as metastasis[17–19]. To examine whether the infection of *F. nucleatum* is correlated with tumor hypoxia, we acclimated CT26FL3 (RFP/Luc) cells to either 1% (hypoxia) or 20% oxygen (normoxia) for 24 h (Fig. 2a). CT26FL3 (RFP/Luc) cells were MSS and mismatch repair (MMR) proficient with close mutational signatures to the wild-type CT26 cells (Supplementary Fig. 3a–c). *F. nucleatum* was able to invade hypoxic CT26FL3 (RFP/Luc) tumor cells (Fig. 2b) with 15-fold higher signals in comparison to cells in normoxia (Fig. 2c). Intracellular *F. nucleatum* was confirmed by stacking images highlighting the co-localization of *F. nucleatum* and phalloidin-labeled F-actin, which showed that *F. nucleatum* was able to invade inside the cytoskeleton in response to hypoxia (Fig. 2d). In *F. nucleatum*-infected CT26FL3 (RFP/Luc) spheroids, bacteria not only adhered to the surface but also translocated into the organoids (Fig. 2e and Supplementary Fig. 5a). The data agree with the clinical observation that *F. nucleatum* has a stronger correlation with larger tumors with hypoxic regions[20]. Spontaneous invasion to hypoxic tumor cells was also found in the facultative anaerobic probiotic strain *Escherichia coli* Nissle, which suggests that bacteria preferentially invade hypoxic tumors (Fig. 2f and Supplementary Fig. 6a).

We established CRC in Balb/C mice infected with *F. nucleatum* (Supplementary Fig. 4a). *F. nucleatum* infection led to an over a 30-fold higher tumor growth ratio compared to uninfected controls (Supplementary Fig. 4b–d). *F. nucleatum* infection considerably promoted tumor metastasis in proximal lymph nodes and distal metastasis (Supplementary Fig. 4e). The primary tumors, distal metastases and feces were confirmed to contain *F. nucleatum* (Supplementary Fig. 4f). There was a considerable increase in anti-inflammatory M2 macrophages and the $CD11b^+Gr1^+$ myeloid-derived suppressor cell (MDSC) population compared to uninfected tumors. An important decrease in the $CD8^+$ T cell population, memory T cells and $CD11c^+MHC\text{-}II^+$ dendritic cells were observed compared to the non-*F. nucleatum*-infected control group (Supplementary Fig. 4g).

Transmission electron microscopy (TEM) images of *F. nucleatum*-infected CRC tumors demonstrated that *F. nucleatum* was intracellular in vivo in the tumor region (Fig. 2g). Fluorescence in situ hybridization (FISH) using an RNA probe specific for the 16S ribosomal RNA (rRNA) of *F. nucleatum* was performed to visualize the bacterium in the CRC tumor sections. The red pixels indicating FISH signals were mapped to the nearest blue pixels indicating DAPI staining, which was calculated by a Euclidean distance map. We further fitted the minimum distance

https://doi.org/10.1038/s41587-023-01957-8

a

Antibiotics	Frequency	Percent
Metronidazole	4,220	95.6%
Clindamycin	75	1.70%
Tinidazole	49	1.11%
Secnidazole	33	0.75%
Clindamycin + metronidazole	22	0.50%
Metronidazole + tinidazole	7	0.16%
Metronidazole + secnidazole	6	0.14%
Tinidazole + secnidazole	1	0.02%
Total	4,413	100%

b

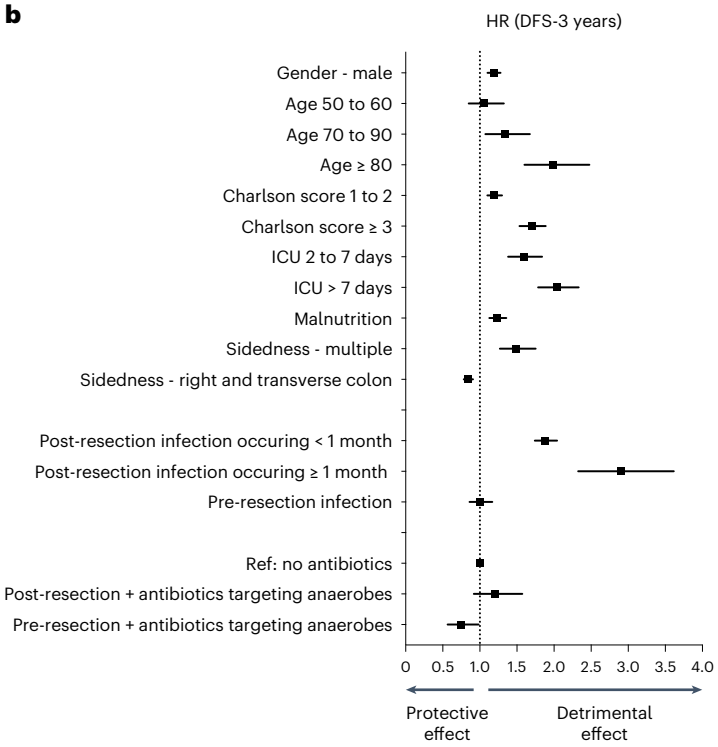

c

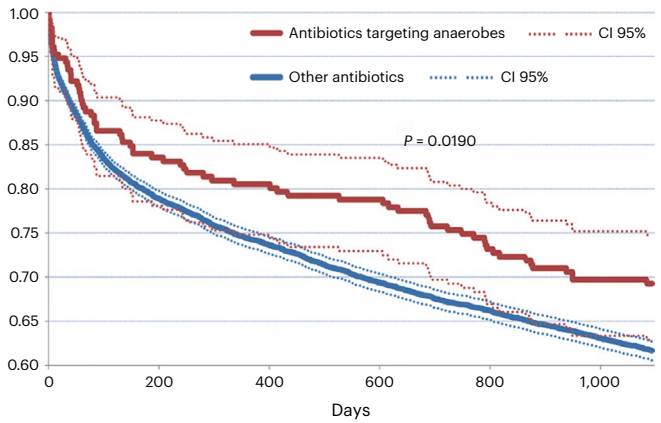

Fig. 1 | The class of antibiotics targeting anaerobic bacteria have protective effect on patients with CRC. a, List of antibiotics that were administered to the cohort and the proportion of the patients who received each drug. **b**, Multivariate analyses by Cox model representing a summary of the maximum likelihood estimates for each variable included in the model. **c**, DFS at 3 years (no death or recurrence within 3 years) comparing patients receiving only antibiotics targeting anaerobes or patients receiving other antibiotics before resection of CRC. Dashed lines represent the 95% CI. ICU, intensive care unit.

distribution by computing the percentage of FISH pixels versus distances to DAPI[21], which was within the range of 3 µm, suggesting that *F. nucleatum* appeared near the cell nuclei in the CRC tumor (Fig. 2h,i and Supplementary Fig. 5b,c).

Escherichia coli Nissle 1917 (*E. coli* Nissle) has been widely studied as a probiotic and engineered bacterium that delivers therapeutics to hypoxic tumors[22]. We established orthotopic *E. coli* Nissle-colonized CRC tumors in BALB/c mice (Supplementary Fig. 6b). *E. coli* Nissle colonized in CRC tumors (Supplementary Fig. 6c,d) and fostered an immunosuppressive tumor microenvironment, which may be caused by colibactin, a genotoxin produced by certain *E. coli* strains[23] (Supplementary Fig. 6e).

Liposomal antibiotics eliminated bacteria in the tumor

Because increasing evidence has shown that administration of broad-spectrum antibiotics potentially induces microbiota dysbiosis[24–26], a drug delivery system that efficiently delivers narrow-spectrum antibiotics against the anaerobic bacteria residing in the hypoxic tumor region is needed to reduce damage to the commensal microbiota in the gut. Nitroimidazole is part of a class of antimicrobial prodrugs that is inactive until reduced by the ferredoxin oxidoreductase system in obligate anaerobes[27–29]. The reductive activation of the nitro group is proposed to form the cytotoxic nitro and other free radicals, leading to structural fragmentation and cytotoxicity to DNA[30]. The presence of oxygen tension inhibits the formation of the cytotoxic derivative. Reductive inactivation of the nitro group to the amino group occurs via oxygen-insensitive nitro reductases, rendering nitroimidazole non-toxic[30]. The intrinsic property of hypoxia activation enabled nitroimidazole to specifically clear the anaerobes residing in the hypoxic tumor. The nitroimidazole coordinates via the ring N3 donor atom with a variety of metal ions, including cobalt (II), copper (II), zinc (II) and silver (I) (Supplementary Fig. 7a). Among these metal ions, Ag^+ ions are potent antibacterial agents used in various forms as antibiotics for centuries[31]. Silver nanoparticles may have the ability to adhere and penetrate the bacterial cell wall[32]. The silver (I) ions interact with sulfur and phosphorus, thereby causing altered activity of enzymes and DNA[33]. The formation of the silver-tinidazole complex was confirmed by mass spectrometry[34–36] (Supplementary Fig. 7b).

Tumor hypoxia directly correlates with tumor acidosis due to the Warburg effect favored by cancer cells that metabolized pyruvate into lactate and ethanol[37]. The low pH of hypoxic tumors as a result of elevated levels of lactic acid may allow drug release in anerobic bacteria residing in the region of the tumor. Inspired by the established metal gradient used for remote loading of chelate complexes into liposomes[38], we hypothesized and demonstrated that the metal ions can be trapping agents for loading nitroimidazole into liposomes (Fig. 3a). The silver-tinidazole complex disassociated in acid, showing the same protonation of both TNZ and AgTNZ as the ring N3 donor atom in acidic medium at pH 4, a condition expected when liposomes enter cellular endosomes and lysosomes (Fig. 3b). The liposomes were spherical with a diameter of ~150 nm and a zeta potential of approximately −13.8 mV as determined by a nanoparticle tracking system (Supplementary Fig. 7c,d). The liposomes were uniform in morphology as imaged by cryogenic electron microscopy (cryo-EM) (Fig. 3c). The loading of TNZ into silver-containing liposomes was efficient with more than 80% encapsulation efficiency and more than 5% loading content (Fig. 3d). TNZ showed quick loading kinetics into the liposomes, over 80% of which were entrapped within 5 min (Fig. 3e). The TNZ-to-Ag ratio in the liposomes was 1.54 ± 0.18 ($n = 4$). This is lower than the theoretical ratio of 2, indicating that the liposomes contained some free

https://doi.org/10.1038/s41587-023-01957-8

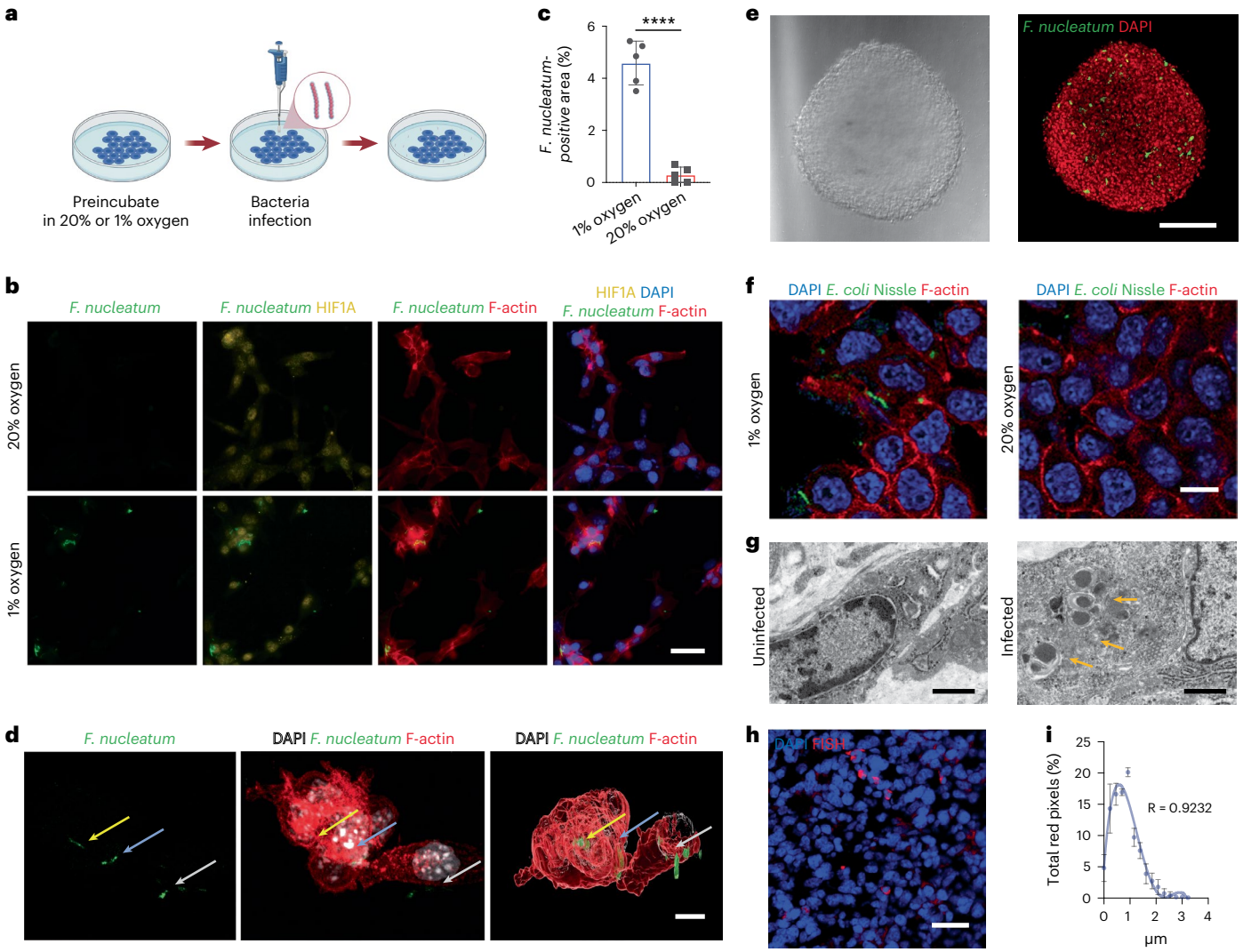

Fig. 2 | *F. nucleatum* invaded CT26FL3(Luc/RFP) tumor cells in response to hypoxia. a, Illustration of *F. nucleatum* infection of CT26FL3(Luc/RFP) cells in vitro. **b**, CFSE-labeled *F. nucleatum* invaded hypoxic CT26FL3(Luc/RFP) cells within a 4-h co-incubation. Scale bar, 20 μm. **c**, Quantification of the *F. nucleatum*-positive area by CFSE fluorescence. $n = 5$ experiments. Data are the mean ± s.d. ****$P < 0.0001$. **d**, Three-dimensional reconstruction of the *z* projection of stacked images of *F. nucleatum*-infected CT26FL3(Luc/RFP) cells. The three arrows in assorted colors indicate intracellular *F. nucleatum*. Scale bar, 5 μm. A video illustrating the spatial distribution of intracellular *F. nucleatum* is provided in Supplementary Video 1. **e**, *F. nucleatum* invaded into three-dimensional spheroids in hypoxia. *z*-stack image of CT26FL3(Luc/RFP) spheroids co-incubated with *F. nucleatum*. *F. nucleatum* covalently labeled by CFSE mostly appeared in intra-spheroid. The left panel is the bright-field optical image of the spheroid. $n = 3$ experiments. Scale bar, 100 μm. **f**, CFSE-labeled *E. coli* Nissle invaded hypoxic CT26FL3(Luc/RFP) cells. $n = 2$ experiments. Scale bar, 10 μm. **g**, TEM Images of CRC tumor sections. Yellow arrows indicate intracellular *F. nucleatum*. $n = 3$ experiments. Scale bar, 1 μm. **h**, FISH visualizing *F. nucleatum* 16S RNA in mouse CRC tumor sections. Scale bar, 20 μm. **i**, Fitting distribution of the minimum distance of *F. nucleatum* to the cell nucleus for each pixel. $n = 4$ experiments.

Ag (I) and/or one-to-one complex. Copper (II) also formed a complex with tinidazole and encapsulated TNZ (Supplementary Fig. 7e). This liposome platform will provide a versatile approach to load nitroimidazole antibiotics targeting anaerobic bacteria in infected tumors. The liposomes dispersed in PBS at pH 7 were stable in 4 days (Supplementary Fig. 7f), and less than 10% of liposome cargoes were released in 30 h (Supplementary Fig. 7g). The bond between silver and tinidazole readily dissociates in acid, as the ring N3 donor atom (pKa = 4.7) was protonated at pH 4.5 (Fig. 3f). The data suggest that liposomes should be stable in systemic circulation without release of the antibiotic cargo.

Antimicrobial assays were performed to determine the minimum inhibitory concentration (MIC) for *F. nucleatum* by plating and enumerating viable colony-forming units (CFU). The AgTNZ complex inhibited *F. nucleatum* with an MIC_{95} of approximately 100 nM (Supplementary Fig. 7h). CT26FL3(Luc/RFP) cells were infected with *F. nucleatum* and incubated with different concentrations of free AgTNZ or LipoAgTNZ for 12 h, and intracellular bacteria were quantified by CFU. Both LipoAgTNZ and free AgTNZ showed higher antimicrobial efficacy in hypoxia. The effective clearance concentration of intracellular *F. nucleatum* in hypoxia was 1.5 μM for LipoAgTNZ versus 7.5 μM for AgTNZ (Fig. 3g) due to the enhanced intracellular accumulation mediated by liposome delivery (Fig. 3h). Therefore, the liposomal formulation has the potential to facilitate intracellular *F. nucleatum* clearance.

To further profile the pharmacokinetic profiles in vivo, intravenous (i.v.)-injected LipoAgTNZ was analyzed by sampling blood from mice bearing orthotopic tumors at predetermined timepoints. The molar ratio of TNZ and Ag remained consistent (approximately 1.5 to 2) within the first 240 min in blood circulation. Compared to the free drug, liposomal TNZ showed superior pharmacokinetic profiles,

https://doi.org/10.1038/s41587-023-01957-8

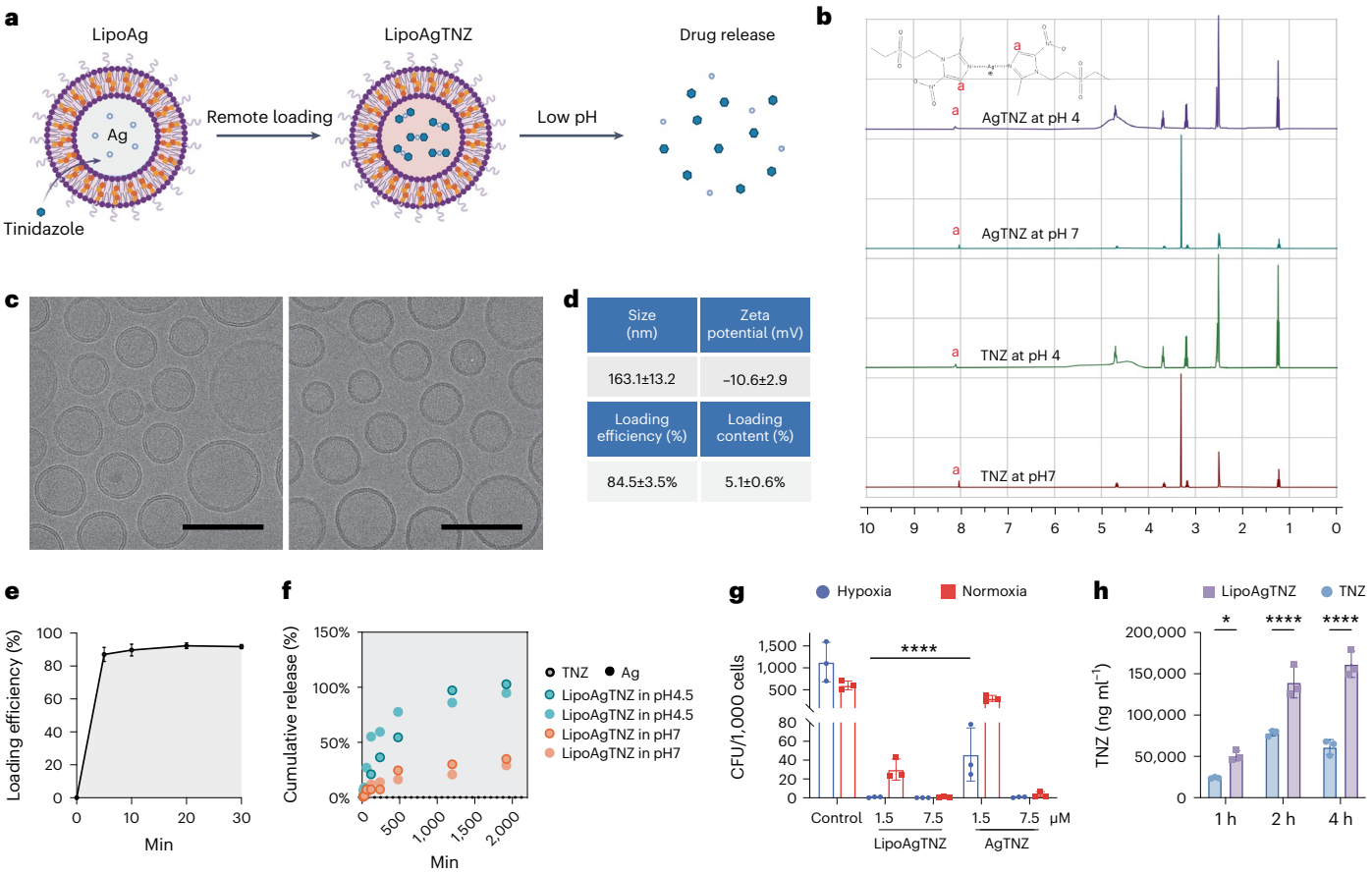

Fig. 3 | Characterization of the pH-sensitive antibiotic liposomes. **a**, Illustration of remote loading by a silver nitrate gradient and drug release in response to low pH. **b**, The ^{1}H nuclear magnetic resonance (NMR) characterization in neutral pH and weak acid. $n = 2$ experiments. **c**, Cryo-EM images of LipoAg and LipoAgTNZ. $n = 3$ experiments. Scale bar, 200 nm. **d**, Summary of loading properties. $n = 3$ experiments. Data are the mean ± s.d. **e**, Loading kinetics of LipoAgTNZ. $n = 3$ experiments. Data are the mean ± s.d. **f**, pH-sensitive drug release of LipoAgTNZ at pH 4.5 and pH 7. Ag and TNZ were determined by ICP–MS and LC–MS, respectively. $n = 2$ experiments. **g**, Intracellular *F. nucleatum* killing by free AgTNZ and LipoAgTNZ under normoxia and hypoxia. $n = 3$ experiments. Data are the mean ± s.d. ****$P < 0.0001$. **h**, In vitro cell uptake of liposomes and free drug at 1 h, 2 h and 4 h. $n = 3$ experiments. Data are the mean ± s.d. *$P < 0.05$; ****$P < 0.0001$.

as indicated by an increasing area under the curve (AUC) of the drug concentration in circulation (Supplementary Fig. 8a,b). Tinidazole is metabolized mainly by CYP3A4 (ref. 39), which supported the higher level and longer half-life ($t_{1/2}$) of silver than TNZ in the tissues and blood (Supplementary Fig. 8c). Liposomes were labeled with DiD, a fluorescent dye that labels the lipid membrane of liposomes. The distribution of liposomes was determined by quantifying DiD fluorescence in the organs. The liposomes mainly localized to the tumor and the liver, as shown by ex vivo images (Supplementary Fig. 8d). Liposomes increased TNZ accumulation in the tumor by more than 10-fold (Supplementary Fig. 8e). Mice were killed at 24 h after i.v. injection of free drug and liposomes. All major organs including the tumor were harvested, homogenized and measured for both drug contents for biodistribution. Tinidazole encapsulated in liposomes mainly accumulated in the tumor at 24 h after i.v. injection, which suggests the success of tumor targeting (Supplementary Fig. 8f).

We performed MTT assays to analyze the in vitro cytotoxicity. Free Ag, TNZ and AgTNZ did not affect the viability of CT26FL3 (Luc/RFP) cells within 48 h of incubation at concentrations as high as 40 μM (Supplementary Fig. 9a,b). For the in vivo toxicity study of liposomal metal-imidazole complexes, healthy (non-tumor-bearing) mice were i.v. injected (4 mg kg^{-1} with respect to TNZ) with either LipoCuTNZ or LipoAgTNZ three times every third day. Treated mice showed no body weight change (Supplementary Fig. 9c). Major organs from tumor-bearing mice were dissected, fixed, embedded in paraffin and examined for tissue histology after treatments. Histological changes related to toxicity were not found among the main organs (Supplementary Fig. 9d). However, metastatic lesions (yellow arrows in the figure) were found in both the control and free TNZ groups. *F. nucleatum* inoculation by oral gavage increased blood platelets, which decreased in response to the LipoAgTNZ treatment. Interestingly, neutrophils—phagocytes decreased by bacterial infection—were considerably elevated in the blood after LipoAgTNZ treatment (Supplementary Fig. 9e). Toxicity biomarkers were assessed, and no obvious alterations in serum biomarkers were observed compared to the untreated mice (Supplementary Fig. 9f).

Killing intracellular bacteria improved immune surveillance

The infected CRC mouse model was used to test the therapeutic efficacy of the antibiotic liposomes. Balb/C mice orthotopically inoculated with tumors and additionally infected with *F. nucleatum* or *E. coli* Nissle received antibiotic liposome treatments (4.0 mg kg^{-1} TNZ and 1.1 mg kg^{-1} Ag, i.v.) (Fig. 4a). Although the growth of *F. nucleatum*-infected tumors was inhibited by both LipoAgTNZ and LipoCuTNZ at day 23 (Fig. 4b and Supplementary Fig. 10a,b), which eradicated the tumor-colonizing bacteria (Fig. 4c), LipoAgTNZ induced long-term survival in six of seven mice (Fig. 4d). We did not observe bacteria colonization in the main organs of mice treated with LipoAgTNZ (Supplementary Fig. 10c).

https://doi.org/10.1038/s41587-023-01957-8

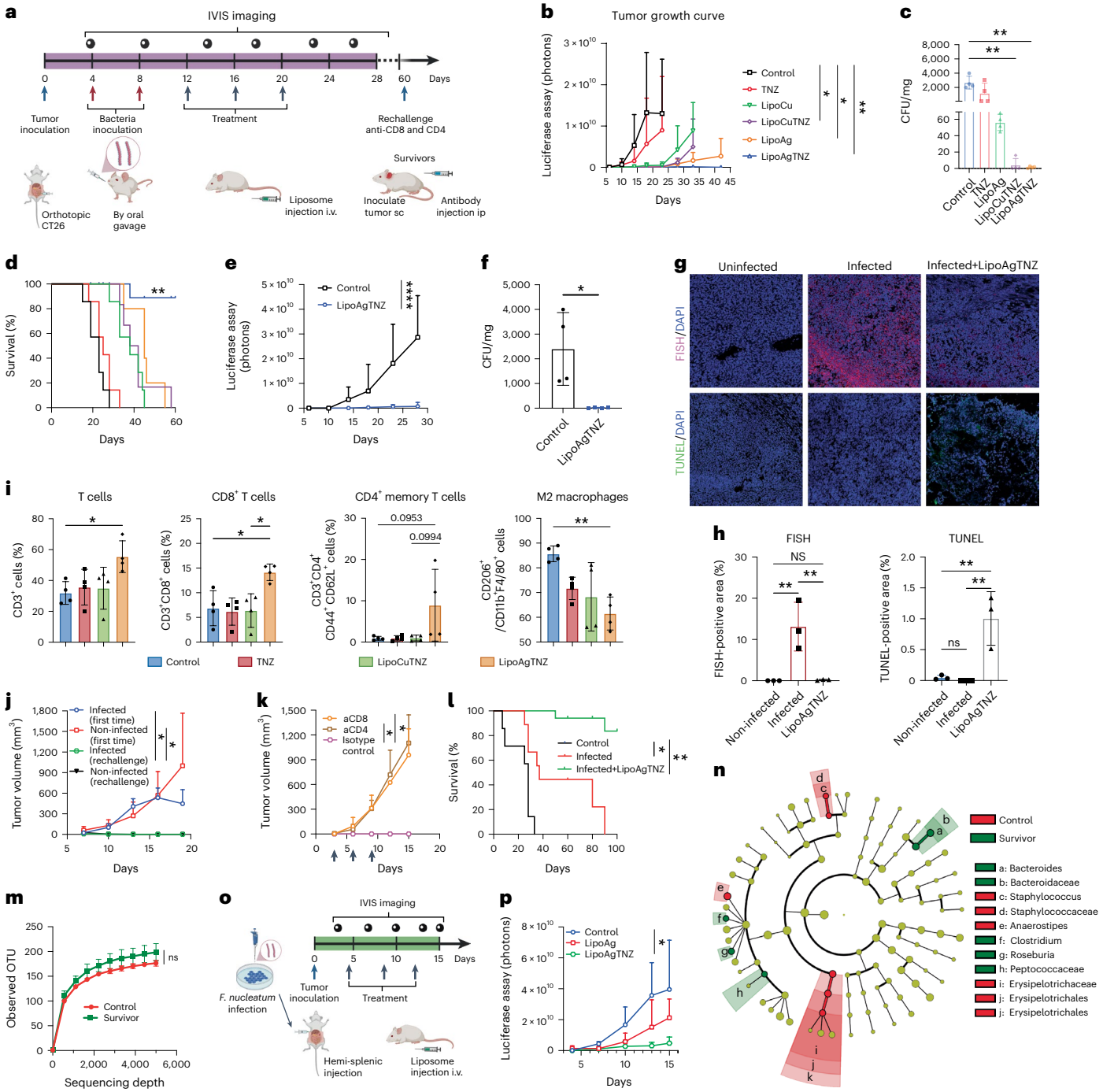

Fig. 4 | Removing *F. nucleatum* in the tumor by liposomal antibiotics AgTNZ eradicated CRC. a, Schematic timeline of the *F. nucleatum*-infected CT26FL3(Luc/RFP) tumor study followed by three doses of LipoAgTNZ treatment. **b**, Tumor growth was monitored by IVIS imaging at six predetermined timepoints. $n = 5$ per group. Data are the mean ± s.d. $^{*}P < 0.05$; $^{**}P < 0.01$. **c**, CFU of *F. nucleatum* in the tumors at day 24. $n = 4$ per group. Data are the mean ± s.d. $^{**}P < 0.01$. **d**, Animal survival curve following the dosing timeline (**a**) from day 0 to day 60. $n = 7$ per group. Data are the mean ± s.d. $^{**}P < 0.01$. **e**, The growth curve of *E. coli Nissle*-infected tumors was monitored by IVIS imaging at six predetermined timepoints. $n = 5$ per group. Data are the mean ± s.d. $^{****}P < 0.0001$. **f**, CFU of *E. coli* Nissle in the tumors at day 24. $n = 4$ per group. Data are the mean ± s.d. $^{*}P < 0.1$. **g**, FISH assays visualizing *F. nucleatum* 16S RNA; TUNEL staining showing apoptosis. $n = 3$ experiments. Scale bar, 20 µm. **h**, Quantification of fluorescence-positive area of **g**. **i**, Analyses of the immune cell population in the tumor microenvironment after treatment. $n = 4$ per group. Data are the mean ± s.d. $^{*}P < 0.05$; $^{**}P < 0.01$. **j**, Tumor growth curve of the rechallenge study. $n = 5$ per group. Data are the mean ± s.d. $^{*}P < 0.05$. **k**, Anti-CD8 and CD4 antibodies were given i.p. after the inoculation of rechallenged tumors as indicated by black arrows. $n = 5$ per group. Data are the mean ± s.d. $^{*}P < 0.05$. **l**, Animal survival curve of *F. nucleatum*-infected MC38 tumor model following the timeline (**a**). **m**, Alpha diversity measuring the microbiome diversity of each sample. $n = 4$ per group. **n**, Linear discriminant analysis effect size (LefSe) to determine the differences at the genus level for significance tests. $n = 4$ per group. Data are the mean ± s.d. NS, not significant. **o**, Scheme of *F. nucleatum*-infected liver metastasis model. The CT26FL3(Luc/RFP) cells were pre-infected with *F. nucleatum* and inoculated into the liver by hemi-splenic injection, followed by three doses of LipoAgTNZ treatment. **p**, Tumor growth curve of CT26FL3(Luc/RFP) liver metastasis. $n = 4$ per group. Data are the mean ± s.d. $^{*}P < 0.05$.

The lipopolysaccharide (LPS) of Gram-negative bacteria was reduced in the tumor after the treatment (Supplementary Fig. 10d). We also tested the approach in the *F. nucleatum*-infected wild-type CT26 tumor model and observed the same tumor and metastasis inhibition with the CT26FL3(Luc/RFP) model (Supplementary Fig. 10e–g). Liposomal AgTNZ was effective in reducing the probiotic *E. coli* Nissle content and inhibiting the growth of infected tumors (Fig. 4e,f). The survival study was also performed in *F. nucleatum*-infected wild-type MC38 tumor-bearing C57BL/6J mice, in which LipoAgTNZ achieved a 71% survival rate (Fig. 4l and Supplementary Fig. 10h) compared to infected mice without treatments.

To test the hypothesis that tumor-associated bacteria are independent of gut-colonized *F. nucleatum*, polymyxin B (pmB) was used to eradicate the Gram-negative bacteria in the gut. pmB is a cyclic peptide with five positive charges and a log(*P*) of −5.6, rendering it low transmembrane permeability and poor oral bioavailability[40]. The orally administered pmB affected the bacteria only in the gut but not in the tumor due to low transmembrane partition and distribution (Supplementary Fig. 10i). The mice treated with pmB did not show a reduction in tumor growth (Supplementary Fig. 10j). We concluded that the tumor colonizing *F. nucleatum* promoted tumor progression, which is independent of the *F. nucleatum* burden in the gut. Interestingly, the efficacy of LipoAgTNZ was dependent on colonization of *F. nucleatum* in the tumor, as the uninfected mice did not respond as well as the infected mice (Supplementary Fig. 10k).

On day 24, tumors were excised and sectioned for the FISH assay using an *F. nucleatum*-specific RNA probe. Consistent with quantification by CFU, FISH signals revealed that LipoAgTNZ effectively reduced the *F. nucleatum* burden in CRC tumors. A TUNEL assay was performed and showed increased apoptotic cells after treatment (Fig. 4g,h). As AgTNZ did not show cytotoxicity to CT26FL3(Luc/RFP) tumor cells (Supplementary Fig. 9a,b), we hypothesized that the treatment induced anti-tumor immunity in immune-competent mice. Infiltration of $CD3^+$ T cells, $CD8^+$ cytotoxic T cells and $CD44^+CD62L^+$ memory T cells was increased in the LipoAgTNZ-treated *F. nucleatum*-infected tumors (Fig. 4i and Supplementary Fig. 11a,b). $CD206^+$ M2 macrophage polarization was reduced after treatment with LipoAgTNZ (Fig. 4i and Supplementary Fig. 11c,d).

To investigate whether the treatment was able to trigger an immune memory response, the long-term survivors were subcutaneously rechallenged with tumor cells with or without *F. nucleatum* infection (Fig. 4a). There was no detectable tumor growth in the survivors but rapid growth in the naive mice (Fig. 4j). The therapeutic efficacy was dependent on the host immune system, as depletion of either CD8 or CD4 cells by antibodies (200 µg per mouse) diminished the anti-tumor activity (Fig. 4k). When mice were examined by necropsy after immune compromise by antibody treatment on day 75, there was no detectable primary tumor left in the long-term survivors (Supplementary Fig. 11e), indicating that the gut tumors were eradicated by the immune response that was dependent on both $CD8^+$ and $CD4^+$ T cells. Therefore, through elimination of the tumor-associated bacteria, the immune-suppressive microenvironment has been turned into an anti-tumoral immune-activated state. CD8 and CD4 cell depletion during primary treatments was performed using the infected CT26FL3(Luc/RFP) model, in which LipoAgTNZ induced tumor inhibition but did not induce long-term survival due to compromised T cell function during treatments (Supplementary Fig. 12a–c).

The FadA adhesin of *F. nucleatum* interacts with E-cadherin, leading to activation of the β-catenin pathway[41]. *F. nucleatum* induces DNA damage, which promotes the release of the cellular tumor suppressor Trp53 (ref. 42). Vimentin is also important in epithelial-to-mesenchymal transition, which is upregulated in *F. nucleatum*-infected tumors[43]. LipoAgTNZ treatment reversed the induction of these metastasis mediators (E-cadherin, Vimentin and β-catenin), Trp53 and the key inflammatory NF-κB pathway in the *F. nucleatum*-infected tumors (Supplementary Fig. 12d).

The clinical treatment for *Fusobacterium* infection is the combination antibiotic therapy consisting of both β-lactam and anaerobic antimicrobial agent[27]. Treatment of the infected CT26FL3(Luc/RFP) tumor with the antibiotic cocktails decreased the tumor; however, cancer relapse occurred after the cocktail treatment (Supplementary Fig. 12a–c). Antibiotic cocktails taken by oral administration non-selectively changed the gut microbiota composition and compromised the immune sensitivity[44,45]. To determine the gut microbiota diversity after LipoAgTNZ treatment, we performed high-throughput gene sequencing analysis of 16S rRNA in fecal bacterial DNA isolated from age-matched control and survivor mice at day 70. Rarefaction analysis comparing bacterial diversity within individual subjects revealed that survivors harbored a similar bacterial community relative to that of controls (Fig. 4m and Supplementary Fig. 13a). These data were further quantified by UniFrac dissimilarity distance analysis (Supplementary Fig. 13b), which was supported by bacterial operational taxonomic composition (Supplementary Fig. 13c). These results support the idea that specific gut microbiota homeostasis was protected by using LipoAgTNZ treatment. To analyze the differentiating bacterial features after antibiotic treatment, linear discriminant analysis effect size (LefSe) was applied to identify the difference in bacterial abundance at the genus level (Fig. 4n and Supplementary Fig. 13d). Interestingly, the enriched bacteria in survivors suggested physiological stress with regard to the abundances of *Peptococcaceae*, *Bacteroidaceae* and *Clostridium*[46]. The increased *Roseburia* produced butyrate, which prevented inflammation and maintained homeostasis in the colon[47].

Liver metastasis, the most common distant metastasis in CRC, afflicts up to 70% of patients[48]. As shown in Supplementary Fig. 8d–f, liposomes predominantly accumulated in the tumor and the liver. We hypothesized that LipoAgTNZ liposomes can efficiently eliminate bacteria in the liver metastasis and induce anti-tumor effects. An *F. nucleatum*-infected liver metastasis model was established (Fig. 4o). The infected tumor cells were inoculated via the portal vein by hemi-splenic injection, which established uniform metastasis in the liver[49]. The development of liver metastasis was inhibited by treatment with LipoAgTNZ (4.0 mg kg^{-1} TNZ and 1.5 mg kg^{-1} Ag, i.v.), as quantified by luciferase imaging in vivo (Fig. 4p and Supplementary Fig. 14a,b). The tumor burdens were reduced by eight-fold at the endpoint, as quantified by ex vivo luciferase signals (Supplementary Fig. 14c,d). FISH imaging for *F. nucleatum* 16S RNA revealed a high abundance of bacteria in the untreated liver metastasis, which was importantly reduced after LipoAgTNZ treatment and associated with enhanced infiltration of $CD8^+$ T cells. LipoAgTNZ treatment also reduced anti-inflammatory M2 macrophages, as CD206 expression was much lower than that in the control group (Supplementary Fig. 14e,f).

Unlike chemotherapy or oncogene-specific therapies that induce cytotoxicity to tumor cells, this strategy targeted the tumor-associated bacteria in the primary tumor and distal metastasis. The process of bacterial killing promoted an anti-cancer response, which restored immune surveillance and inhibited both primary tumor growth and metastatic progression. Thus, it was worthwhile to look for the bacterial epitopes that were recognized by the host immune system.

T cells from long-term survivors showed specificity to both infected and unifected tumors

To analyze T cell specificity to bacterial infection, T cells isolated from survivor mice were compared to those isolated from age-matched uninfected naive mice. Splenic pan T cells were labeled with the proliferation dye CFSE and injected into recipient mice with or without *F. nucleatum* infection. T cell proliferation was found in both infected and uninfected recipient mice that received T cells from survivors but not from naive donors (Fig. 5a,b). Incubating survivor-derived donor

https://doi.org/10.1038/s41587-023-01957-8

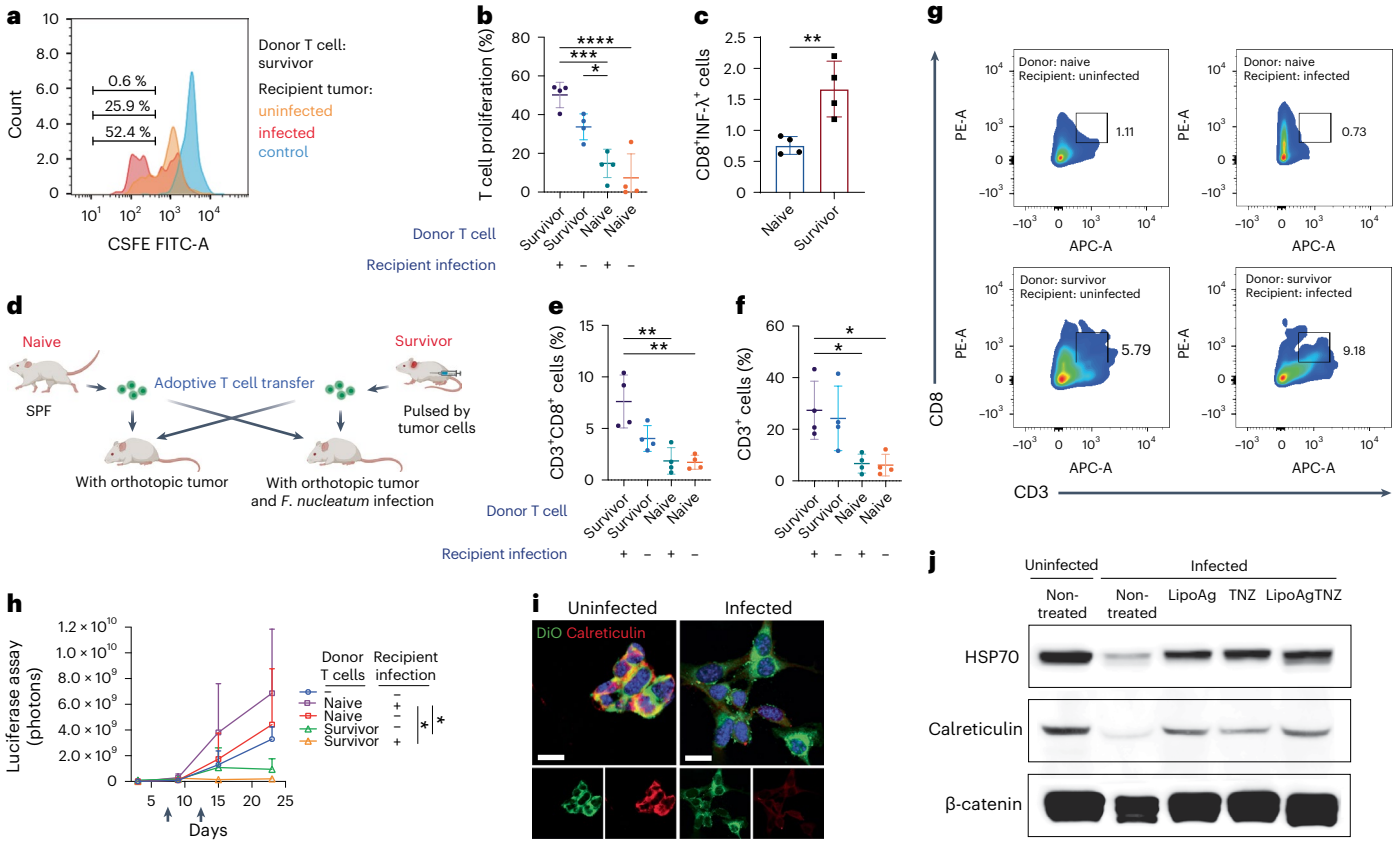

Fig. 5 | T cells from survivors suppressed the growth of both infected and uninfected tumors. a, In vivo T cell proliferation assay. Tumor-infiltrating T cells were isolated from donor splenocytes and labeled with the proliferation dye CFSE before injection into recipient mice. **b**, Quantification of flow cytometry data in **a** of the percentage of proliferated T cells by gating the fluorescence of CFSE level. $n = 4$ per group. Data are the mean ± s.d. $^{*}P < 0.05$; $^{***}P < 0.001$; $^{****}P < 0.0001$. **c**, Lymphocytes were isolated from survivor or naive mice and incubated with CT26FL3(Luc/RFP) cells for 24 h in vitro. Quantification of data of $CD8^{+}IFN\text{-}\gamma^{+}$ T cells after incubation. $n = 4$ per group. Data are the mean ± s.d. $^{**}P < 0.01$. **d**, Illustration of the T cell adoptive transfer study. Mice with orthotopic CRC tumors with or without *F. nucleatum* infection received T cells from either naive mice or long-term survivor mice from LipoAgTNZ treatment as described in Fig. 4a. **e**, Quantification of $CD3^{+}CD8^{+}$ T cells; data shown in **g**. $n = 4$ per group. Data are the mean ± s.d. $^{**}P < 0.01$. **f**, Quantification of $CD3^{+}$ T cells; data also shown in **g**. $n = 4$ per group. Data are the mean ± s.d. $^{*}P < 0.05$. **g**, Representative flow cytometry analysis of $CD3^{+}CD8^{+}$ T cells in tumors of the recipient mice after adoptive T cell transfer. **h**, Donor T cells inhibited tumor growth in recipient mice. $n = 4$ per group. Data are the mean ± s.d. $^{*}P < 0.05$. **i**, Confocal image of immunofluorescence of calreticulin (red) in *F. nucleatum*-uninfected and -infected CT 26(FL3) tumor cells. Scale bar, 5 μm. $n = 3$ experiments. **j**, Chaperon expression induced by killing intracellular bacteria treatment.

T cells with uninfected tumor cells in vitro enhanced $CD8^{+}IFN\text{-}\gamma^{+}$ cell populations (Fig. 5c and Supplementary Fig. 15a). These data suggest that the T cells from the long-term survivors were primed to infected and uninfected tumor cells.

Splenic pan T cells of long-term survivor mice after LipoAgTNZ treatment were adoptively transferred to test the efficacy in recipient mice bearing orthotopic CRC tumors with or without *F. nucleatum* infection (Fig. 5d). Donor T cells from the long-term survivor mice effectively inhibited the growth of tumors infected with *F. nucleatum*; unexpectedly, the same donor T cells also inhibited uninfected tumors (Fig. 5h). Substantially increased numbers of $CD3^{+}$ and $CD3^{+}CD8^{+}$ T cells were found in the tumors of both infected and uninfected mice (Figs 5e–g and Supplementary Fig. 15b,c). The data again suggest that survivor T cells recognized both infected and uninfected tumor cells in vivo in the recipient mice.

F. nucleatum infection decreased the co-localization of calreticulin with the cell membrane, downregulating chaperons (for example, calreticulin) (Fig. 5i). It is likely that this downregulation is a part of the immune suppression mechanism of the infected tumor cells. It is interesting to note that *F. nucleatum* infection in hypoxia downregulated the stress proteins, which are usually upregulated by cells under hypoxic conditions[50,51]. Treatment with LipoAgTNZ in hypoxia restored chaperone by killing intracellular bacteria (Fig. 5j). The result suggested that immunogenic cell death may contribute to immune activation of the tumor cells under the treatment of LipoAgTNZ.

Host T cells specifically targeted bacterial epitopes after antibiotic treatment

The data in Figs. 4 and 5 suggest that LipoAgTNZ induced T cell immunity in CRC-bearing mice. It is worthwhile to identify the epitopes generated by bacterial death. According to the identification of transmembrane helices, 1,171 of 2,067 proteins are cytoplasmic at the *F. nucleatum* subcellular localization in proteome-wide prediction of Vaxign2 (Fig. 6a)[52,53]. To identify the most abundant protein in cytoplasm, the label-free proteomics of *F. nucleatum* was mapped to subcellular localization (Fig. 6a). The proteomics data are generated from the data source of reference papers[54,55]. To estimate the potential neoepitopes, we predicted the MHC-I $H\text{-}2K^{d}$, $H\text{-}2D^{d}$ and $H2L^{d}$ binding peptides from the proteins ranking top in the quantitative proteomics of *F. nucleatum*, followed by selection of the epitopes with high total score and MHC binding affinity (Fig. 6b,d). The top-ranked cytoplasmic proteins in abundance were selected for epitope prediction. Five top-ranked peptides predicted from each protein were selected using the Immune Epitope Database (IEDB) by applying the NetMHCpan

https://doi.org/10.1038/s41587-023-01957-8

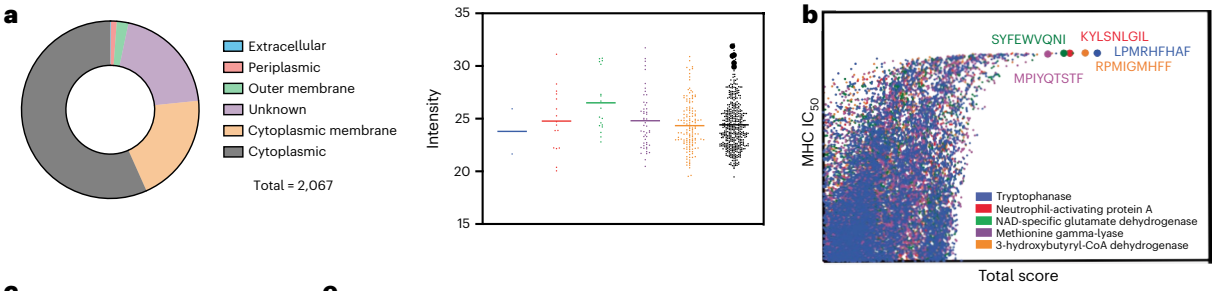

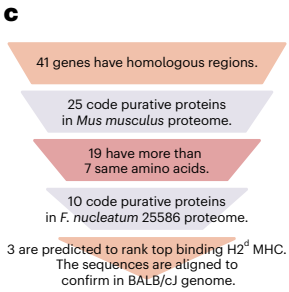

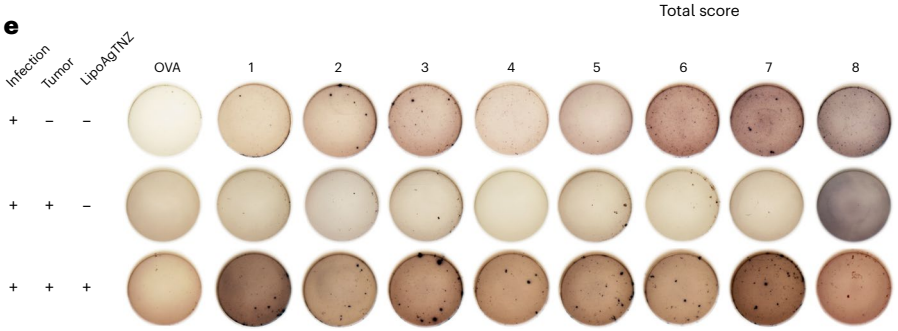

d

Protein	Epitope	Number	Peptide length	Allele	Amino acid matching	Similarity with host	Host protein with similarity
Neutrophil-activating protein A	KYLSNLGIL	1	9	H-2-Kd	9–17	N	N/A
Tryptophanase	LPMRHFHAF	2	9	H-2-Ld	48–56	N	N/A
NAD-specific glutamate dehydrogenase	SYFEWVQNI	3	9	H-2-Kd	368–376	N	N/A
Methionine gamma-lyase	MPIYQTSTF	4	9	H-2-Ld	27–35	N	N/A
3-hydroxybutyryl-CoA dehydrogenase	RPMIGMHFF	5	9	H-2-Ld	9–17	N	N/A
Chaperone protein DnaK	GVPQIEVTF	6	9	H-2-Dd	439–447	Y	Stress-70 protein
Chaperone protein DnaK	RQATKDAGTI	7	10	H-2-Kd	127–136	Y	Endoplasmic reticulum chaperone bip precursor
P-type Ca(2+) transporter	LADDNFSTIV	8	10	H-2-Kd	641–649	Y	Sarcoplasmic/Endoplasmic reticulum calcium atpase 2

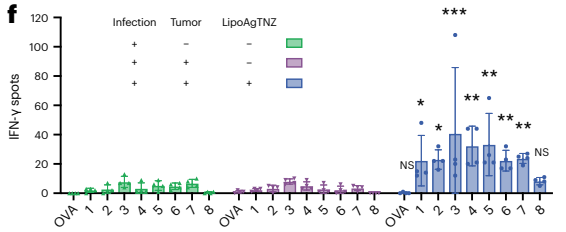

g

Protein	Epitope	Number	Peptide length	Allele	Amino acid matching	Similarity with host	Host protein with similarity
Acetyl-CoA acetyltransferase	VITAFSNI	9	8	H-2-Kb	35–42	N	N/A
Alkyl hydroperoxide reductase C22 protein	SVFVFYPADFTF	10	12	H-2-Kb	36–47	N	N/A
Chaperone protein DnaK	ISLPFITM	11	8	H-2-Kb	252–259	N	N/A
Chaperone protein DnaK	AAIQGGVLM	12	9	H-2-Db	346–354	N	N/A
P-type Ca(2+) transporter	LADDNFSTI	13	9	H-2-Db	36–44	Y	Sarcoplasmic/Endoplasmic reticulum calcium ATPase 2
Chaperone protein DnaK	RGVPQIEVTF	14	10	H-2-Db	11–20	Y	Stress-70 protein

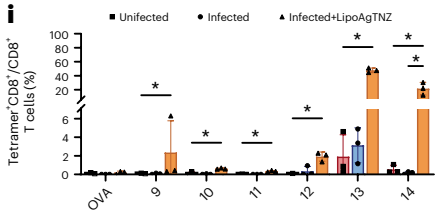

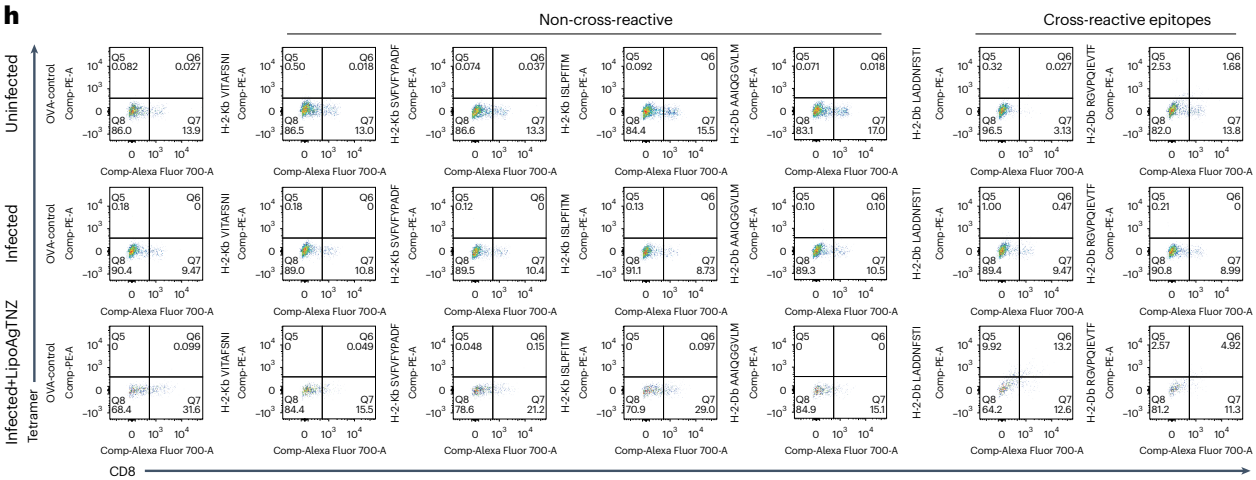

Fig. 6 | The killing of tumor-associated bacteria promoted immune recognition of bacterial neoepitopes. a, Topology analysis of the proteome and proteomics of *F. nucleatum* based on prediction of subcellular localization. The right panel shows label-free quantitative proteomics mapped with predicted subcellular localization. The selected proteins are marked with enlarged black circles. **b**, Scatter plot showing the rank for total scores and peptide–MHC complex affinity. **c**, Filters set for alignment of the *F. nucleatum* and mouse genomes to generate the homologous epitopes. **d**, Information on the selected peptides predicted by the IEDB database. **e**, Representative images of IFN-γ ELISpot. **f**, Quantification of IFN-γ spots. $n = 4$ per group. $^{*}P < 0.05$; $^{**}P < 0.01$; $^{***}P < 0.001$; NS, not significant. **g**, $H2^{b}$ MHC binding *F. nucleatum* epitopes of C57BL6 mice filtered by **c** using the same methods except the selection of MHC haplotypes and reference genome of C57BL6 mice. **h**, Representative flow cytometry analysis of tetramers loaded with bacterial epitopes listed in **g** staining the orthotopic-infected MC38-infiltrating T cell tumor. The establishment of MC38 model with C57BL6 mice is described in Supplementary Fig. 10h and Fig. 4l. **i**, Percentage of tetramer positive CD8+ T cells. $n = 3$ experiments. $^{*}P < 0.05$. IC_{50}, half-maximal inhibitory concentration.

algorithm for mouse MHC-I presentation (sequences shown in the upper-right corner of Fig. 6b).

To explore the homologous antigens shared by bacteria and mice, we aligned the genome of *F. nucleatum* with the mouse genome[56]. Forty-one genes showed similarity, including those in the non-open reading frames. We then selected corresponding proteins from the mice proteome, and 25 proteins were selected, of which only 19 contained potential sequences longer than seven amino acids for the possibility of MHC-I presentation[57]. Ten of 19 sequences encode proteins based on the *F. nucleatum* proteome (Fig. 6c). Interestingly, four similar sequences out of 10 come from the HSP70 chaperon protein (*DnaK* in gene name), which has 65% similarity with mouse HSP70 (Supplementary Table 1). Three epitopes outstand by prediction of the IEDB database according to their likelihood to be presented by $H2K^d$, $H2D^d$ and $H2L^d$, the MHC-I haplotype of the Balb/C strain (Fig. 6d). In summary, peptides 1–5 are bacteria-derived neoantigens sharing no sequence similarity with mice. Peptides 6–8 are homologous epitopes that are shared between bacteria and mice.

To confirm the activity of the peptides in vivo, we recovered splenic $CD8^+$ T cells from Balb/c mice that had survived from CRC tumors infected by *F. nucleatum* after LipoAgTNZ treatment and restimulated them in vitro with the candidate peptides presented by bone-marrow-derived dendritic cells to measure IFN-γ production in an ELISpot assay. Both homologous antigens and neoantigens showed enhanced IFN-γ-secreting T cells after LipoAgTNZ treatment (Fig. 6e,f). Splenic T cells from mice infected with *F. nucleatum* but not treated with LipoAgTNZ did not show a considerable INF-γ response to the bacterial cytoplasmic peptides. A peptide from chicken ovalbumin (OVA) was used as a negative control.

To explore the targets that the T cell receptors recognized after antibiotic treatment, we performed tetramer–peptide complex staining the tumor-infiltrating T cells. Bacterial peptides were loaded to the corresponding H2 haplotype tetramers, and the complex was incubated with T cells isolated from the MC38 tumor (Fig. 6g). Heterologous (peptide 9 and 10), heterologous epitopes from DnaK protein (peptide 11 and 12) and homologous epitopes (peptide 13 and 14) were selected for tetramer staining. The LipoAgTNZ treatment induced higher T cell population recognizing the bacteria peptides (Fig. 6h,i). Data indicated that peptide 13 (LADDNFSTI) and peptide 14 (RGVPQIEVTF) stood out by showing high positive ratio in $CD8^+$ T cell population. The results indicated that the major tumor-infiltrating T cell specificities are against the bacteria–host shared epitopes in the antibiotics-treated group, which induced important response against infected and uninfected tumor cells.

Overall, these data demonstrate that bacteria epitopes can be presented by host MHC-I after LipoAgTNZ treatment. The tolerance of self-epitopes that are shared with the tumor-associated bacteria is likely reversed by the danger signals induced by the killing of intracellular bacteria.

Bacteria-derived epitopes have been found to elicit anti-cancer immunity. Fecal microbiota transplantation improved the immune microenvironment and improved the checkpoint inhibitor response in immunotherapy-refractory patients with melanoma[58]. Bacteria-derived HLA-bound peptides were recently identified in tumors from patients with melanoma[6]. Memory responses by IFN-γ-expressing $CD4^+$ and $CD8^+$ T cells specific for *Enterococcus hirae*, *Bacteroides fragilis* and *Akkermansia muciniphila* have been associated with favorable clinical outcomes in patients with cancer[59–61].

The data suggest that T cells from survivors established long-term anti-tumor efficacy compared to T cells from naive mice. These LipoAgTNZ-treated mice developed IFN-γ^+CD8^+ T cells in response to bacteria-derived neoantigens. Interestingly, IFN-γ^+ CD8 T cells in response to homologous epitopes also developed after antibiotic treatment, suggesting cellular immunity against the self-epitopes. This result is consistent with the T cell transfer study in which T cells from survivor mice suppressed uninfected tumor growth. We predominantly analyzed bacteria-induced $CD8^+$ T cells in response to class I MHC antigens, which is the cytotoxic T cell phenotype for anti-tumor efficacy, whereas $CD4^+$ T cells in response to class II MHC antigens were reported to generate either cytotoxicity or tolerance[62,63].

Discussion

Personalized cancer vaccines under development aim to direct the immune system against the unique neoantigen repertoire of an individual's tumor. This process is dependent on sufficient neoantigen quantity and quality in addition to adequate immune functionality. Killing of tumor-associated bacteria may contribute a new source of neoantigens to facilitate homologous and neoepitope-mediated cellular immunity against CRC.

Our work stemmed from the observation that antibiotics targeting anaerobic bacteria extended the DFS of patients with CRC and infected mice. In patients with colon cancers, the benefit derived from antibiotics was limited to pre-resection intake, suggesting that the quantity of intratumoral bacteria to prime immunity may be crucial to success. These results pave the way for neoadjuvant clinical interventions with targeted antibiotics specific to the intratumoral microbiota combined with immunotherapy to boost anti-tumor immunity. Dedicated prospective studies categorizing intratumoral bacteria, tumoral stage and the optimal timing and impact of antibiotics are needed before clinical implementation.

Anti-tumoral immune response relies on the ability of immune cells to recognize and eliminate tumor-derived antigens. Mutation-derived neoantigens are recognized as a major determinant to benefit from immunomodulating strategies. The lack of mutation-derived neoantigens, as in most MSS CRCs, associated with an immunosuppressive microenvironment is a major barrier to developing long-term anti-tumoral immunity. To decipher the intertwinement between anti-tumoral immunity, the gut microbiome and antibiotic treatment, we developed liposomes remotely loaded with antibiotics to target the CRC tumors. We showed that intratumoral pro-tumoral bacteria established in an immunosuppressed tumoral milieu can be targeted by antibiotics to induce the release of cancer-specific microbial neoantigens. We performed adoptive T cell transfer and T cell epitope studies to investigate the function of the immune system after bacterial removal. The treatment induced infiltration of cytotoxic $CD8^+$ T cells in the tumor, which has specificity to microbial neoepitopes. Homologous epitopes also showed anti-tumor efficacy, which may result in an immune response to uninfected tumors. Thus, the killing of tumor-associated bacteria can turn an immunologically cold tumor into a hot tumor and prime the immune system to recognize both infected and uninfected tumor cells. The discovery of cancer-associated microbial neoantigens offers exciting possibilities for the development of innovative anti-tumoral therapeutic or preventive vaccine strategies.

Online content

Any methods, additional references, Nature Portfolio reporting summaries, source data, extended data, supplementary information, acknowledgements, peer review information; details of author contributions and competing interests; and statements of data and code availability are available at https://doi.org/10.1038/s41587-023-01957-8.

References

1. Bodinier, M. et al. Efficient detection and immunomagnetic sorting of specific T cells using multimers of MHC class I and peptide with reduced CD8 binding. *Nat. Med.* **6**, 707–710 (2000).
2. Alard, E. et al. Advances in anti-cancer immunotherapy: CAR-T cell, checkpoint inhibitors, dendritic cell vaccines, and oncolytic viruses, and emerging cellular and molecular targets. *Cancers (Basel)* **12**, 1826 (2020).

3. Le, D. T. et al. PD-1 blockade in tumors with mismatch-repair deficiency. *N. Engl. J. Med.* **372**, 2509–2520 (2015).
4. Nejman, D. et al. The human tumor microbiome is composed of tumor type-specific intracellular bacteria. *Science* **368**, 973–980 (2020).
5. Fluckiger, A. et al. Cross-reactivity between tumor MHC class I-restricted antigens and an enterococcal bacteriophage. *Science* **369**, 936–942 (2020).
6. Kalaora, S. et al. Identification of bacteria-derived HLA-bound peptides in melanoma. *Nature* **592**, 138–143 (2021).
7. Yang, Y. et al. Focused specificity of intestinal T_H17 cells towards commensal bacterial antigens. *Nature* **510**, 152–156 (2014).
8. Zheng, D.-W. et al. Phage-guided modulation of the gut microbiota of mouse models of colorectal cancer augments their responses to chemotherapy. *Nat. Biomed. Eng.* **3**, 717–728 (2019).
9. Goodman, A. L. & Gordon, J. I. Our unindicted coconspirators: human metabolism from a microbial perspective. *Cell Metab.* **12**, 111–116 (2010).
10. Kostic, A. D. et al. Genomic analysis identifies association of *Fusobacterium* with colorectal carcinoma. *Genome Res.* **22**, 292–298 (2012).
11. Sepich-Poore, G. D. et al. The microbiome and human cancer. *Science* **371**, eabc4552 (2021).
12. Derosa, L. et al. Microbiota-centered interventions: the next breakthrough in immuno-oncology? *Cancer Discov.* **11**, 2396–2412 (2021).
13. Song, M., Chan, A. T. & Sun, J. Influence of the gut microbiome, diet, and environment on risk of colorectal cancer. *Gastroenterology* **158**, 322–340 (2020).
14. Poore, G. D. et al. Microbiome analyses of blood and tissues suggest cancer diagnostic approach. *Nature* **579**, 567–574 (2020).
15. Rousseau, B. et al. Impact of antibiotics (ATB) on the recurrence of resected colorectal cancer (CRC): results of EVADER-1 a nation-wide pharmacoepidemiologic study. *J. Clin. Oncol.* **38**, 4106 (2020).
16. Sargent, D. J. et al. A pooled analysis of adjuvant chemotherapy for resected colon cancer in elderly patients. *N. Engl. J. Med.* **345**, 1091–1097 (2001).
17. Castellarin, M. et al. *Fusobacterium nucleatum* infection is prevalent in human colorectal carcinoma. *Genome Res.* **22**, 299–306 (2012).
18. Bullman, S. et al. Analysis of *Fusobacterium* persistence and antibiotic response in colorectal cancer. *Science* **358**, 1443–1448 (2017).
19. Zhou, Z., Chen, J., Yao, H. & Hu, H. *Fusobacterium* and colorectal cancer. *Front. Oncol.* **8**, 371 (2018).
20. Brennan, C. A. & Garrett, W. S. *Fusobacterium nucleatum*—symbiont, opportunist and oncobacterium. *Nat. Rev. Microbiol.* **17**, 156–166 (2019).
21. Sun, Y. et al. Adaptive-guided-coupling-probability level set for retinal layer segmentation. *IEEE J. Biomed. Health Inform.* **24**, 3236–3247 (2020).
22. Canale, F. P. et al. Metabolic modulation of tumours with engineered bacteria for immunotherapy. *Nature* **598**, 662–666 (2021).
23. Wilson, M. R. et al. The human gut bacterial genotoxin colibactin alkylates DNA. *Science* **363**, eaar7785 (2019).
24. Riquelme, E. et al. Tumor microbiome diversity and composition influence pancreatic cancer outcomes. *Cell* **178**, 795–8062 (2019).
25. Ahn, J. et al. Human gut microbiome and risk for colorectal cancer. *J. Natl Cancer Inst.* **105**, 1907–1911 (2013).
26. Pinato, D. J. et al. Association of prior antibiotic treatment with survival and response to immune checkpoint inhibitor therapy in patients with cancer. *JAMA Oncol.* **5**, 1774–1778 (2019).
27. Arane, K. & Goldman, R. D. *Fusobacterium* infections in children. *Can. Fam. Physician* **62**, 813–814 (2016).
28. Leitsch, D. et al. Pyruvate:ferredoxin oxidoreductase and thioredoxin reductase are involved in 5-nitroimidazole activation while flavin metabolism is linked to 5-nitroimidazole resistance in *Giardia lamblia*. *J. Antimicrob. Chemother.* **66**, 1756–1765 (2011).
29. Upcroft, P. & Upcroft, J. A. Drug targets and mechanisms of resistance in the anaerobic protozoa. *Clin. Microbiol. Rev.* **14**, 150–164 (2001).
30. Dingsdag, S. A. & Hunter, N. Metronidazole: an update on metabolism, structure–cytotoxicity and resistance mechanisms. *J. Antimicrob. Chemother.* **73**, 265–279 (2018).
31. Qiu, K., Durham, P. G. & Anselmo, A. C. Inorganic nanoparticles and the microbiome. *Nano Res.* **11**, 4936–4954 (2018).
32. Kim, D. et al. Selective killing of pathogenic bacteria by antimicrobial silver nanoparticle–cell wall binding domain conjugates. *ACS Appl. Mater. Interfaces* **10**, 13317–13324 (2018).
33. Prabhu, S. & Poulose, E. K. Silver nanoparticles: mechanism of antimicrobial action, synthesis, medical applications, and toxicity effects. *Int. Nano Lett.* **2**, 32 (2012).
34. Waszczykowska, A., Żyro, D., Ochocki, J. & Jurowski, P. Clinical application and efficacy of silver drug in ophthalmology: a literature review and new formulation of EYE drops with drug silver (I) complex of metronidazole with improved dosage form. *Biomedicines* **9**, 210 (2021).
35. Starek, M., Dąbrowska, M., Chebda, J., Żyro, D. & Ochocki, J. Stability of metronidazole and its complexes with silver(I) salts under various stress conditions. *Molecules* **26**, 3582 (2021).
36. Radko, L., Stypuła-Trębas, S., Posyniak, A., Żyro, D. & Ochocki, J. Silver(I) complexes of the pharmaceutical agents metronidazole and 4-hydroxymethylpyridine: comparison of cytotoxic profile for potential clinical application. *Molecules (Basel)* **24**, 1949 (2019).
37. Vander Heiden, M. G., Cantley, L. C. & Thompson, C. B. Understanding the Warburg effect: the metabolic requirements of cell proliferation. *Science* **324**, 1029–1033 (2009).
38. Yu, J. et al. Remote loading paclitaxel–doxorubicin prodrug into liposomes for cancer combination therapy. *Acta Pharm. Sin. B* **10**, 1730–1740 (2020).
39. Guo, G., Guo, T. & Chang, X. Effect of CYP3A4 genetic polymorphisms on pharmacokinetics of tinidazole. *Journal of Chinese Pharmaceutical Sciences* **29**, 272–279 (2020).
40. Sivanesan, S. et al. Pharmacokinetics of the individual major components of polymyxin B and colistin in rats. *J. Nat. Prod.* **80**, 225–229 (2017).
41. Rubinstein, M. R. et al. *Fusobacterium nucleatum* promotes colorectal carcinogenesis by modulating E-cadherin/β-catenin signaling via its FadA adhesin. *Cell Host Microbe* **14**, 195–206 (2013).
42. Geng, F., Zhang, Y., Lu, Z., Zhang, S. & Pan, Y. *Fusobacterium nucleatum* caused DNA damage and promoted cell proliferation by the *Ku70/p53* pathway in oral cancer cells. *DNA Cell Biol.* **39**, 144–151 (2020).
43. Zhang, S. et al. *Fusobacterium nucleatum* promotes epithelial-mesenchymal transiton through regulation of the lncRNA MIR4435-2HG/miR-296-5p/Akt2/SNAI1 signaling pathway. *FEBS J.* **287**, 4032–4047 (2020).
44. Park, E. M. et al. Targeting the gut and tumor microbiota in cancer. *Nat. Med.* **28**, 690–703 (2022).
45. Smith, M. et al. Gut microbiome correlates of response and toxicity following anti-CD19 CAR T cell therapy. *Nat. Med.* **28**, 713–723 (2022).
46. Lobionda, S., Sittipo, P., Kwon, H. Y. & Lee, Y. K. The role of gut microbiota in intestinal inflammation with respect to diet and extrinsic stressors. *Microorganisms* **7**, 271 (2019).

47. Nie, K. et al. *Roseburia intestinalis*: a beneficial gut organism from the discoveries in genus and species. *Front. Cell. Infect. Microbiol.* **11**, 757718 (2021).
48. Okano, K., Shimoda, T. & Matsumura, Y. Clinicopathologic and immunohistochemical study of early colorectal cancer with liver metastases. *J. Gastroenterol.* **34**, 334–340 (1999).
49. Goodwin, T. J., Zhou, Y., Musetti, S. N., Liu, R. & Huang, L. Local and transient gene expression primes the liver to resist cancer metastasis. *Sci. Transl. Med.* **8**, 364ra153 (2016).
50. Han, Y. K. et al. Hypoxia induces immunogenic cell death of cancer cells by enhancing the exposure of cell surface calreticulin in an endoplasmic reticulum stress-dependent manner. *Oncol Lett.* **18**, 6269–6274 (2019).
51. Cao, J. et al. Heat shock protein 70 attenuates hypoxiainduced apoptosis of pulmonary microvascular endothelial cells isolated from neonatal rats. *Mol. Med. Rep.* **24**, 690 (2021).
52. He, Y., Xiang, Z. & Mobley, H. L. Vaxign: the first web-based vaccine design program for reverse vaccinology and applications for vaccine development. *J. Biomed. Biotechnol.* **2010**, 297505 (2010).
53. Ong, E. et al. Vaxign2: the second generation of the first Web-based vaccine design program using reverse vaccinology and machine learning. *Nucleic Acids Res.* **49**, W671–W678 (2021).
54. Ali Mohammed, M. M., Pettersen, V. K., Nerland, A. H., Wiker, H. G. & Bakken, V. Label-free quantitative proteomic analysis of the oral bacteria *Fusobacterium nucleatum* and *Porphyromonas gingivalis* to identify protein features relevant in biofilm formation. *Anaerobe* **72**, 102449 (2021).
55. Mohammed, M. M. A., Pettersen, V. K., Nerland, A. H., Wiker, H. G. & Bakken, V. Quantitative proteomic analysis of extracellular matrix extracted from mono- and dual-species biofilms of *Fusobacterium nucleatum* and *Porphyromonas gingivalis*. *Anaerobe* **44**, 133–142 (2017).
56. Cameron, M. & Williams, H. E. Comparing compressed sequences for faster nucleotide BLAST searches. *IEEE/ACM Trans. Comput. Biol. Bioinform.* **4**, 349–364 (2007).
57. Stevens, J., Wiesmüller, K.-H., Walden, P. & Joly, E. Peptide length preferences for rat and mouse MHC class I molecules using random peptide libraries. *Eur. J. Immunol.* **28**, 1272–1279 (1998).
58. Gil-Cruz, C. et al. Microbiota-derived peptide mimics drive lethal inflammatory cardiomyopathy. *Science* **366**, 881–886 (2019).
59. Sato, T. et al. Single Lgr5 stem cells build crypt-villus structures in vitro without a mesenchymal niche. *Nature* **459**, 262–265 (2009).
60. LeBlanc, D. J., Lee, L. N. & Abu-Al-Jaibat, A. Molecular, genetic, and functional analysis of the basic replicon of pVA380-1, a plasmid of oral streptococcal origin. *Plasmid* **28**, 130–145 (1992).
61. Kennedy, M. J. et al. Rapid blue-light-mediated induction of protein interactions in living cells. *Nat. Methods* **7**, 973–975 (2010).
62. Krienke, C. et al. A noninflammatory mRNA vaccine for treatment of experimental autoimmune encephalomyelitis. *Science* **371**, 145–153 (2021).
63. Hu, Z. et al. Personal neoantigen vaccines induce persistent memory T cell responses and epitope spreading in patients with melanoma. *Nat. Med.* **27**, 515–525 (2021).

[1]Division of Pharmacoengineering and Molecular Pharmaceutics, Eshelman School of Pharmacy, University of North Carolina, Chapel Hill, NC, USA. [2]Department of Medicine, Memorial Sloan Kettering Cancer Center, New York, NY, USA. [3]Lineberger Comprehensive Cancer Center, University of North Carolina, Chapel Hill, NC, USA. [4]Department of Genetics, University of North Carolina, Chapel Hill, NC, USA. [5]Department of Microbiology and Immunology, University of North Carolina, Chapel Hill, NC, USA. [6]Department of Bioinformatics and Computational Biology, University of North Carolina, Chapel Hill, NC, USA. [7]Health Data and Assessment Department, Data Science and Assessment Division, French National Cancer Institute, Boulogne-Billancourt, France. [8]Natural Products Research Laboratories, Eshelman School of Pharmacy, University of North Carolina, Chapel Hill, NC, USA. [9]Chinese Medicine Research and Development Center, China Medical University and Hospital, Taichung, Taiwan. [10]Curriculum in Oral and Craniofacial Biomedicine, Division of Oral and Craniofacial Health Sciences, Adams School of Dentistry, University of North Carolina, Chapel Hill, NC, USA. [11]Thurston Arthritis Research Center, Division of Rheumatology, Allergy, and Immunology, University of North Carolina, Chapel Hill, NC, USA. [12]Department of Radiology and Biomedical Research Imaging Center, University of North Carolina, Chapel Hill, NC, USA. [13]Health Survey, Data Science and Assessment Division, French National Cancer Institute, Boulogne Billancourt, France. [14]GERCOR Group, Paris, France. [15]Medical Oncology Department, Curie Institute, Saint Cloud, France. [16]Residual Tumor & Response to Treatment Laboratory, RT2Lab, Translational Research Department, INSERM, U932 Immunity and Cancer, Paris, France. [17]INSERM, U900, Paris, France. [18]MINES ParisTech, PSL Research University, CBIO-Centre for Computational Biology, Paris, France. [19]Department of Medical Oncology, Centre René Hughenin, Saint Cloud, France. [20]Department of Surgery, Institut Jean Godinot, Reims, France. [21]Department of Surgical Oncology, Institut Curie, University of Paris, Paris, France. [22]BMTCT Program, Division of Hematology, Lineberger Comprehensive Cancer Center, University of North Carolina, Chapel Hill, NC, USA. [23]Department of Internal Medicine, University of North Carolina, Chapel Hill, NC, USA. [24]Key Laboratory of Polymer Ecomaterials, Changchun Institute of Applied Chemistry, Chinese Academy of Sciences, Changchun, China. [25]Jilin Biomedical Polymers Engineering Laboratory, Changchun, China. [26]Center for Gastrointestinal Biology and Disease, University of North Carolina, Chapel Hill, NC, USA. [27]Department of Computational Medicine and Bioinformatics, University of Michigan, Ann Arbor, MI, USA. [28]Unit for Laboratory Animal Medicine, University of Michigan Medical School, Ann Arbor, MI, USA. [29]Department of Microbiology and Immunology, University of Michigan Medical School, Ann Arbor, MI, USA. [30]Division of Craniofacial and Surgical Care, School of Dentistry, University of North Carolina at Chapel Hill, Chapel Hill, NC, USA. ✉e-mail: leafh@email.unc.edu

Methods

Selection criteria of the clinical cohort

The specific methodology regarding the colorectal cohort and antibiotic consumption was previously reported[15]. In brief, the present study included all people aged 18 years or older with incident non-metastatic CRC resected between January 2012 and December 2014 in France. To select incident cases, we excluded people with a previous history of cancer (2010–2011) or long-term disease for cancer (diagnosed before 2012). To obtain a homogeneous population with the same study duration, each patient was followed up for 3 years after surgical resection. The 3-DFS is a validated criterion for adjuvant studies and an accepted surrogate for overall survival in CRC.

Measurement of antibiotic therapy in the clinical cohort

All reimbursements for antibiotics were extracted during the perioperative period of 6 months before the surgical resection and until 1 year after. We assumed that each pill delivered was taken by the patient. We used the daily delivery dose of each antibiotic to convert the quantity reimbursed in number of days of treatment. Because drugs dispensed during a hospitalization were not directly traceable in the cancer cohort, the consumption of antibiotics in the hospital has been evaluated by the presence of a diagnostic code (ICD-10) for infectious diseases. Hospital infections occurring after surgery were split into those occurring within 30 d and those occurring more than 30 d after surgery to isolate postoperative infections.

For outpatient consumption of antibiotics targeting anaerobes, we predefined a list of antibiotics approved for the treatment of *Fusobacterium nucleatum* spp.-related infection using Anatomical Therapeutic Chemical codes as follows: (1) nitroimidazole: metronidazole, tinidazole, nimorazole, ornidazole and secnidazole; and (2) lincosamides: clindamycin and lincomycin.

Covariates used in the multivariate model

Several potentially predictive factors for survival were identified or reconstructed from the available data: sex, age (18–49, 50–69, 70–79 and ≥80 years), laterality of cancer Charlson comorbidity index (none, 1–2 and ≥3), nutritional status during the surgical resection (malnutrition versus no malnutrition), admission to the intensive care unit during the surgical resection length of stay (no admission or <2 d, 2–7 d and >7 d) and time when antibiotics were used along the time axis to account for a potential time-dependent bias.

Identification of recurrences in the clinical cohort

Recurrences were identified by an algorithm looking for the occurrence of an ICD-10 diagnostic code for metastases, a palliative care code, a new cancer-related surgical resection after the first one or treatment with chemotherapy or radiotherapy starting more than 3 months after the surgical resection.

Statistical analysis of clinical data

3-DFS was defined as the time elapsed between the date of surgery (time origin) and the date of recurrence, death or the end of 3-year follow-up, whichever occurred first. The 3-year DFS was modeled using Cox models to study the link with antibiotics intake adjusted for all covariates.

The survival curves are represented using the Kaplan–Meier method and compared with the log-rank test. HRs were estimated by Cox proportional regression models. As this study was conducted in the overall population (not a sample), statistical tests for descriptive comparisons were not considered relevant. Antibiotic exposure before T0 was considered a fixed variable. Antibiotic exposure after T0 was considered a time-dependent variable[64]. A multivariate model was carried out to isolate the effect of antibiotics targeting anaerobes by comparing patients who received only these antibiotics to those who did not receive any antibiotics as outpatients.

Cell lines

Metastatic CT26FL3 cells were kindly provided by Maria Marjorette O. Peña at the University of South Carolina. CT26FL3(Luc/RFP) cells stably expressing red fluorescent protein (RFP) and luciferase (Luc) were established by transfection with lentivirus vectors carrying RFP and Luc genes and a puromycin resistance gene. CT26FL3(RFP/luc) cells were cultured in DMEM with 4.5 g L^{-1} glucose (Gibco) and 10% BCS (HyClone) supplemented with 1 µg ml^{-1} puromycin (Thermo Fisher Scientific) and 1% antibiotic-antimycotic (Gibco) at 37 °C and 5% CO_2 in a humidified atmosphere. MC38 cells were purchased from Kerafast and cultured in DMEM with 10% BCS, 0.1 mM non-essential amino acids and 1% antibiotic-antimycotic.

Animal models

All animal handling protocols were approved by the University of North Carolina at Chapel Hill's Institutional Animal Care and Use Committee. Six-to-eight-week-old female BALB/cJ or C57BL/6J mice were obtained from The Jackson Laboratory. Animals were maintained in a specific pathogen-free facility (12-h light/dark cycle, tempeature 21–23 °C, humidity 30–70%). All mice were used at 6–8 weeks of age and were age and sex matched for the experiment.

The orthotopic and subcutaneous CT26(FL3)-RFP/Luc tumor model was established based on previous work[65,66]. In brief, female BALB/cJ mice were anesthetized with 2.5% isoflurane in oxygen in the supine position. A midline incision was made to exteriorize the cecum. CT26(FL3)-RFP/Luc cells at a density of 2.0×10^6 in 50 µl of mixture of PBS and Matrigel (1:1) were injected into the cecum wall. The cecum was returned to the peritoneal cavity before the incision was sutured. The tumor burden was monitored by bioluminescent analysis using an IVIS imager (PerkinElmer) with intraperitoneal (i.p.) injection of 100 µl of D-luciferin (PerkinElmer, 10 mg ml^{-1}). Each mouse was inoculated with 10^8 CFU of *F. nucleatum* in 100 µl of PBS every fifth or fourth day by oral gavage.

The subcutaneous tumor model was established by injection of 1.0×10^6 CT26(FL3)-RFP/Luc cells in 100 µl of PBS into the right flank of the BALB/cJ mice. The rechallenge studies were performed by subcutaneously inoculating 10^6 tumor cells. CT26(FL3)-RFP/Luc was infected with *F. nucleatum* before inoculation. Tumor volume (V_t) was calculated as follows:

$$V_t = 0.5 \times a \times b^2 \quad (1)$$

In equation (1), a and b are defined as the major and minor diameter of the tumor.

Liver metastasis model was previously reported[49,67]. CT26(FL3)-RFP/Luc was infected with *F. nucleatum* before inoculation. Female BALB/cJ mice were anesthetized with 2.5% isoflurane in oxygen in the supine position. An incision was made to exteriorize the spleen below the left rib cage. The spleen was tied and cut into two parts that contain intact vascular pedicle for each half. The distal section of the spleen was inoculated with 1.0×10^6 CT26(FL3) cells in 150 µl of PBS. The hemi-spleen containing inoculated cells was resected 5 min after inoculation, allowing the cancer cells to enter the liver through the portal vein. The other half of the spleen was returned to the peritoneal cavity, and the incision was sutured. The tumor burden was monitored by bioluminescent analysis using an IVIS imager (PerkinElmer, Living Image version 4.5) with i.p. injection of 100 µl of D-luciferin (PerkinElmer, 10 mg ml^{-1}). For ex vivo imaging, the dissected liver with tumor was quickly rinsed in PBS and placed in diluted luciferin solution (1 mg ml^{-1}) for 1 min. Bioluminescence imaging was applied immediately.

In vitro cell infection

Five milliliters of overnight *F. nucleatum* or *E. coli* Nissle culture was harvested and washed in sterile PBS two times by centrifugation at 4,000 r.p.m. for 10 min in an anaerobic chamber. The optical density was adjusted to 1.3×10^9 CFU per milliliter. For intracellular bacterial

imaging, the bacteria were then stained with 5 μM CFSE (Invitrogen) according to the manufacturer's instructions. The culture medium of CT26FL3(Luc/RFP) cells was changed to DMEM supplemented with 10% BCS without antibiotics before bacterial infection. The cells were then incubated with the stained or unstained bacteria at a multiplicity of infection (MOI) of 20 in a hypoxic incubator for 4 h, followed by three washes in PBS. The cells were harvested for inoculation. For intracellular bacteria imaging, the cells were stained with phalloidin and antibodies as described below. Antibodies (Supplementary Table 2) were incubated at 4 °C overnight.

Liposome preparation

Distearoyl phosphatidylcholine (16.0 mg, Avanti), cholesterol (10.0 mg, Avanti) and 1,2-distearoyl-sn-glycero-3-phosphoethanolamine-N-[methoxy (polyethylene glycol)-2000] (5.0 mg, Avanti) were dissolved in chloroform. The solvent was evaporated to form a lipid thin film. Three milliliters of 300 mM silver nitrate solution (adjusted to pH 3.0 with nitric acid) was added to hydrate the film at 65 °C for 15 min, and then the suspension was sequentially extruded through 400-nm, 200-nm and 100-nm membranes for 10 times. Gel filtration (Sephadex G-50) was used to remove the silver ions from the outer aqueous phase of the liposomes and to replace it with 5% sucrose with EDTA (UltraPure, pH 8.0, 1:25 dilution by sucrose solution) and then with 5% glucose without EDTA. The liposomes were incubated with tinidazole (0.4 mg) at 65 °C for 15 min for remote loading. The gel filtration was repeated to remove the unencapsulated tinidazole. For analysis, the drug-loaded liposomes were dissolved in methanol and measured by liquid chromatography with mass spectrometry (LC–MS) and inductively coupled plasma mass spectrometry (ICP–MS) for tinidazole and Ag^{+}, respectively. Liposomal encapsulation efficiency was calculated as the weight of tinidazole entrapped in liposomes versus the total weight of tinidazole added. Liposomal loading efficiency was calculated as the weight of tinidazole entrapped in liposomes versus the weight of gross materials added.

FISH

F. nucleatum in orthotopic CRC tissues was determined using RNA in situ hybridization. The *F. nucleatum* 16S RNA probe was synthesized by GenScript. The sequence of the *F. nucleatum*-targeted RNA probe was 5′-CUUGUAGUUCCGCrYUACCUC/3′CY5/-3′ with a CY5 label at the 3′ end, which was based on a previously reported *F. nucleatum*-targeted probe (S-G-Fuso-0664-a-A-19, https://probebase.csb.univie.ac.at/pb_report/probe/1346)[68]. Stellaris RNA FISH buffers (Stellaris RNA FISH Wash Buffer A, Stellaris RNA FISH Wash Buffer B and Stellaris RNA FISH Hybridization Buffer) were used according to the Stellaris RNA FISH protocol for frozen tissue. In brief, fresh dissected tumors were quickly embedded in Tissue-Plus O.C.T. Compound and stored at −80 °C. The frozen tumors were sliced at a thickness of 10 μm, fixed with 4% paraformaldehyde and permeabilized with 70% ethanol. The slices were subsequently immersed in Wash Buffer A for 5 min, dispensed with 200 μl of Hybridization Buffer containing a probe solution of 125 nM, followed by incubation in dark at 37 °C for 16 h. The slides were then incubated with Wash Buffer A in dark for 30 min, stained with 5 μg ml^{-1} DAPI in Wash Buffer A, immersed in Wash Buffer B for 5 min and mounted with Prolong Diamond Antifade Mountant (Thermo Fisher Scientific). We stained uninfected tumors with the probes as negative controls to verify that the FISH assay specifically detected *F. nucleatum*. Images were acquired by Zeiss ZEN 2011.

FISH quantification

The distance map indicating the minimum distance between FISH signals and DAPI staining was calculated by the Euclidean distance function:

$$d(x) = \min(||x - y||), x \in \Omega_F, y \in \Omega_D \quad (2)$$

where Ω_F and Ω_D are the image domains of FISH signals and DAPI staining, respectively. x/y denotes the position of each pixel in the two-dimensional coordinate system. For each x of FISH signals, we computed its minimum distance from the position of DAPI staining by equation (2). x and $d(x)$ were then fitted with a polynomial fourth-order curve to better reflect the correlation of the distance between FISH signals and DAPI staining, by GraphPad Prism 9.0 software.

Fecal DNA isolation and library preparation

Mouse stool samples were collected on day 60 after LipoAgTNZ treatment and immediately stored at −80 °C upon collection. Fecal DNA was isolated using a QIAamp Fast DNA Stool Mini Kit (Qiagen) following the manufacturer's protocol. Then, 12.5 ng of total DNA was amplified by polymerase chain reaction (PCR) using primer set (515F-806R)[69,70] targeting the V4 region on 16S rRNA genes, and PCR amplicons were sequenced at the V4 region on an Illumina MiSeq (Illumina). Subsequently, each sample was amplified using a limited cycle PCR program, adding Illumina sequencing adapters and dual-index barcodes (index 1(i7) and index 2(i5)) (Illumina) to the amplicon target. The final libraries were purified using AMPure XP reagent (Beckman Coulter), quantified and normalized before pooling. The DNA library pool was then denatured with NaOH, diluted with hybridization buffer and heat denatured before loading on the MiSeq reagent cartridge (Illumina) and on the MiSeq instrument (Illumina). Automated cluster generation and paired-end sequencing with dual reads were performed according to the manufacturer's instructions.

Bioinformatic analysis

Sequencing output from the Illumina MiSeq platform was converted to FASTQ format and demultiplexed using Illumina Bcl2Fastq 2.20.0. The resulting paired-end reads were processed with the Quantitative Insights Into Microbial Ecology (QIIME) 2 2021-2 (ref. 71) wrapper for DADA2 (ref. 72) including merging paired ends, quality filtering, error correction and chimera detection. Amplicon sequencing units from DADA2 were assigned taxonomic identifiers with respect to the Greengenes[73] and Silva[74] databases; their sequences were aligned using maFFT[75] in QIIME 2; and a phylogenetic tree was built with FastTree[76] in QIIME 2. A rarefaction curve was generated at a depth of 5,000 sequences per subsample. β-diversity estimates were calculated within QIIME 2 using weighted UniFrac between samples at a subsampling depth of 5,000. The results were summarized and visualized through principal coordinate analysis as implemented in QIIME 2. Microbiota taxonomy was also applied to classify the organism as a representative operational taxonomic unit (OTU). The linear discriminant analysis effect size (LEfSe) Galaxy module was used for analysis examining biologic consistency and effect relevance (http://huttenhower.sph.harvard.edu/galaxy)[77], which was conducted by coupling standard tests for statistical significance.

T cell isolation and adoptive transfer

The spleens from long-term survivors (pulsed with 2×10^6 CT26FL3 (Luc/RFP) cells subcutaneously in the lower right flank 48 h before T cell isolation) and naive mice were disassociated in PBS with 0.1% BSA and 2 mM EDTA using a syringe plunger and filtered through a 40-μm cell strainer. The splenocytes were centrifuged at 300*g* for 10 min at 4 °C and washed in 50 ml of PBS with 0.1% BSA and 2 mM EDTA. The cells were resuspended with 10 ml of RPMI 1640 medium (Gibco) with 120 Kunitz units per milliliter of DNase for 15 min at room temperature and filtered through a cell strainer. The cells were washed with 50 ml of PBS with 0.1% BSA and 2 mM EDTA, resuspended in 4 ml of PBS with 0.1% BSA and 2 mM EDTA and purified by 3 ml of Ficoll-Paque PLUS at 400*g* for 30–40 min at room temperature. The undisturbed lymphocytes at the interface were collected and used for in vivo (CFSE-labeled cells) and in vitro T cell proliferation assays.

Pan T cells were further isolated by negative magnetic labeling using a pan T cell isolation kit (Miltenyi Biotec). T cells were treated

with biotin–antibody cocktail and subsequently anti-biotin cocktail and separated by an LS column (Miltenyi Biotec) in elution buffer (PBS with 0.5% BSA and 2 mM EDTA) in the magnetic field of the MACS separator (Miltenyi Biotec). The cells were adjusted to 1×10^6 in 200 µl of PBS and i.v. injected into the recipient mice on day 10 and day 15 after tumor inoculation.

Bacteria epitope prediction

For bacteria-derived neoantigens, cytoplasmic proteins of *F. nucleatum* were predicted by Vaxign2 (https://violinet.org/vaxign2) and then ranked by the abundance in the quantitative label-free proteomics[54,55]. The most abundent proteins were selected for T cell epitope prediction. T cell epitopes were predicted using open-source tools based on artificial neural networks supported by IEDB (https://iedb.org/) and NetMHC 4.0 server (http://www.cbs.dtu.dk/services/NetMHC/). MHC haplotypes corresponding to strain Balb/C and C57BL/6 were used for this exercise. Predicted epitopes were ranked, and potential epitopes were used for T cell study.

For bacteria-derived homologous antigens: To explore the homologous antigens shared by bacteria and mice, the genome of *Fusobacterium nucleatum subsp. nucleatum* ATCC 25586 (GCA_000007325.1) was aligned with the mice genome (GRCm39 reference annotation release 109) by using Nucleotide Blast[56]. The putative proteins in mouse proteome were selected, among which sequences longer than seven amino acids were further filtered and aligned in *F. nucleatum* proteome (UP000002521_190304). The homologous peptide sequences were selected for T cell epitope prediction.

ELISpot assay

ELISpot assay was used to test the memory immune response and MHC-restricted peptides on splenic $CD8^+$ T cells. IFN-γ ELISpot assays (R&D Systems, EL485) were performed in 96-well sterile plates. The membrane of plates was precoated with capture IFN-γ antibody and incubated with blocking buffer for 2 h. Bone-marrow-derived dendritic cells (10^5 per well) were pulsed with peptides (20 µg ml^{-1}) and added to $CD8^+$ T cells (2×10^4 per well) for 24 h at 37 °C, and plate areas were developed with a biotinylated detection antibody specific for IFN-γ for 1 h, followed by streptavidin–alkaline phosphatase for 1 h. Finally, the substrate of alkaline phosphatase (BCIP/NBT buffer) was added for 5–20 min. Spots were imaged by using stereomicroscopy (Olympus BX61).

Tetramer study

After 28 d of orthotopic tumor inoculation, surface immunophenotyping of tumor-infiltrating T lymphocytes was performed as follows. Single-cell suspension of solid tumor was obtained by standard Ficoll-Paque density gradient centrifugation. $CD8^+$ T lymphocytes were isolated by negative bead selection (Miltenyi Biotec, 130-104-075). The T cell epitopes were evaluated for the percentage of specific $CD8^+$ T lymphocytes by staining with an H2-Db- or H2-Kb-peptide tetramer (5001-1-20, Eagle Biosciences) and anti-CD8 monoclonal antibody.

Statistical analysis

Statistical analysis comparing two groups was performed using an unpaired two-tailed *t*-test. Comparisons between three or more groups were performed using ordinary two-way ANOVA with multiple comparisons. For survival analyses, the log-rank test was used for comparison. All statistical analyses were performed using GraphPad Prism 9.0.1 and 9.5.1 software. Appropriate tests were applied in analyzing these data, meeting assumptions of the statistical methods. A *P* value less than 0.05 was considered significant. Data are presented as the means ± s.d.

Reporting summary

Further information on research design is available in the Nature Portfolio Reporting Summary linked to this article.

Data availability

The 16S rRNA data are available through the National Center for Biotechnology Information (NCBI) Sequence Read Archive (accession numbers SRR23197060–SRR23197067, BioProject PRJNA926798). The whole-exome sequencing data are available through the Sequence Read Archive (BioProject PRJNA926643). The genome of *Fusobacterium nucleatum subsp. nucleatum* ATCC 25586 (GCA_000007325.1) is available on KEGG (https://www.genome.jp/kegg-bin/show_organism?org=fnu). *Mus musculus* genome (GRCm39 reference annotation release 109) is available at the NCBI (https://www.ncbi.nlm.nih.gov/genome/annotation_euk/Mus_musculus/109/). *Fusobacterium nucleatum reference proteome* (UP000002521_190304) is available at the European Bioinformatics Institute (https://www.ebi.ac.uk/reference_proteomes/). All other data supporting the findings of this study are available from the corresponding authors upon reasonable request. Source data are provided with this paper.

Code availability

The distance map for FISH images analysis is available on Zenodo (https://doi.org/10.5281/zenodo.8200515)[78].

References

64. Munoz-Price, L. S., Frencken, J. F., Tarima, S. & Bonten, M. Handling time-dependent variables: antibiotics and antibiotic resistance. *Clin. Infect. Dis.* **62**, 1558–1563 (2016).
65. Song, W. et al. Trapping of lipopolysaccharide to promote immunotherapy against colorectal cancer and attenuate liver metastasis. *Adv. Mater.* **30**, e1805007 (2018).
66. Song, W. et al. Synergistic and low adverse effect cancer immunotherapy by immunogenic chemotherapy and locally expressed PD-L1 trap. *Nat. Commun.* **9**, 2237 (2018).
67. Hu, M. et al. Relaxin gene delivery mitigates liver metastasis and synergizes with check point therapy. *Nat. Commun.* **10**, 2993 (2019).
68. Gmur, R., Wyss, C., Xue, Y., Thurnheer, T. & Guggenheim, B. Gingival crevice microbiota from Chinese patients with gingivitis or necrotizing ulcerative gingivitis. *Eur. J. Oral Sci.* **112**, 33–41 (2004).
69. Caporaso, J. G. et al. Global patterns of 16S rRNA diversity at a depth of millions of sequences per sample. *Proc. Natl Acad. Sci. USA* **108**, 4516–4522 (2011).
70. Mohsen, A., Park, J., Chen, Y. A., Kawashima, H. & Mizuguchi, K. Impact of quality trimming on the efficiency of reads joining and diversity analysis of Illumina paired-end reads in the context of QIIME1 and QIIME2 microbiome analysis frameworks. *BMC Bioinformatics* **20**, 581 (2019).
71. Caporaso, J. G. et al. QIIME allows analysis of high-throughput community sequencing data. *Nat. Methods* **7**, 335–336 (2010).
72. Callahan, B. J. et al. DADA2: high-resolution sample inference from Illumina amplicon data. *Nat. Methods* **13**, 581–583 (2016).
73. DeSantis, T. Z. et al. Greengenes, a chimera-checked 16S rRNA gene database and workbench compatible with ARB. *Appl. Environ. Microbiol.* **72**, 5069–5072 (2006).
74. Quast, C. et al. The SILVA ribosomal RNA gene database project: improved data processing and web-based tools. *Nucleic Acids Res.* **41**, D590–D596 (2013).
75. Katoh, K. & Standley, D. M. MAFFT multiple sequence alignment software version 7: improvements in performance and usability. *Mol. Biol. Evol.* **30**, 772–780 (2013).
76. Price, M. N., Dehal, P. S. & Arkin, A. P. FastTree 2—approximately maximum-likelihood trees for large alignments. *PLoS ONE* **5**, e9490 (2010).
77. Segata, N. et al. Metagenomic biomarker discovery and explanation. *Genome Biol.* **12**, R60 (2011).

78. Sun, Y. et al. Killing tumor-associated bacteria with a liposomal antibiotic generates microbial neoantigens that induce anti-tumor immune responses. (2023). https://zenodo.org/record/8200515

Acknowledgements

K.-H.L. passed away before the submission of the manuscript. The paper is dedicated in memory of him. We thank the University of North Carolina's Department of Chemistry Mass Spectrometry Core Laboratory, especially E. D. Weatherspoon, for assistance with mass spectrometry analysis. We thank the University of North Carolina's Department of Microscopy Services Laboratory, especially V. J. Madden, for assistance with TEM imaging. We thank the University of North Carolina's Animal Histopathology and Laboratory Medicine Core, especially L. Wang, for assistance with histology and toxicity analysis. We thank the University of North Carolina's Cryo-EM Core, especially J. Peck, for assistance with cryo-EM imaging. We thank the University of North Carolina's Nanomedicines Characterization Core Facility, especially M. Sokolsky, for assistance with ICP–MS analysis. We thank the University of North Carolina's Microbiome Core Facility for 16S rRNA gene sequencing, the Cancer Center Support Grant (P30 CA016086) and the Center for Gastrointestinal Biology and Disease (P30 DK34987). Figures 2a, 3a, 4a, 4o and 5d and Supplementary Figs. 4a, 6b, 10h and 12a were created with BioRender. The work was supported by NIH grant CA198999 (to L.H. and A.A.), the Fred Eshelman Distinguished Professorship (to L.H.), the Institut National du Cancer (InCa), the Nuovo-Soldati Foundation, Swim Across America and, in part, through NIH/NCI Cancer Center Support Grant P30 CA008748 (to B.R., M.B.F. and O.A.). M.B.F. is funded by NIH T32-CA009512 and an ASCO Young Investigator Award.

Author contributions

L.H., A.A. and M.W. conceived and designed the research. L.H., M.W., K.Q., A.V., A.A., W.S., J.G., J.A., J.N. and J.P.-Y.T. designed the experiments and analyzed the data. B.R., C.L.B.-B., I.K., P.-J.B., M.H., M.F., E.D., A.H. and F.R. generated the database and did methodology, statistical analyses, models and figures for clinical data. O.A. analyzed the whole-genome sequencing data. K.Q. established the culture and plating system for *F. nucleatum* and modeled the growth curve versus turbidity. G.H. did sample preparation and data analysis for 16S rRNA sequencing. H.S. aligned epitopes from bacteria proteome. Y.H. ran the topology analysis for bacteria genome. Y.-Y.C., K.-H.L. and M.W profiled the pharmacokinetics of the drugs. Y.Z., Y.L. and M.W. sampled the tissues and serum for pharmacokinetic and toxicity assays. M.M. did deconvolution and reconstruction of the images. Y.S. coded for the FISH quantification. J.G., X.Z., Y.Z. and M.W. performed the surgery and in vivo mouse experiments. X.Z. and M.W. did flow cytometry analysis. L.L., P.A. and M.W. purified and analyzed T cell epitopes. M.W. and Y.Z. prepared the frozen sections and immunofluorescence, FISH staining and qPCR assays. M.W., B.R. and L.H. wrote the manuscript.

Competing interests

L. Huang: Consultant with PDS Biotechnology and Stemirna Therapeutics. B. Rousseau: Advisory/Consultancy, Speaker Bureau/Expert testimony: Bayer; Advisory/Consultancy, Speaker Bureau/Expert testimony: Roche; Travel/Accommodation/Expenses: Servier; Travel/Accommodation/Expenses: Astellas; Speaker Bureau/Expert testimony: Gilead.

Additional information

Supplementary information The online version contains supplementary material available at https://doi.org/10.1038/s41587-023-01957-8.

Correspondence and requests for materials should be addressed to Leaf Huang.

Peer review information *Nature Biotechnology* thanks the anonymous reviewers for their contribution to the peer review of this work.

nature portfolio

Corresponding author(s): *Double-blind peer review submissions: write DBPR and your manuscript number here instead of author names.*

Last updated by author(s): *YYYY-MM-DD*

Reporting Summary

Nature Portfolio wishes to improve the reproducibility of the work that we publish. This form provides structure for consistency and transparency in reporting. For further information on Nature Portfolio policies, see our Editorial Policies and the Editorial Policy Checklist.

Statistics

For all statistical analyses, confirm that the following items are present in the figure legend, table legend, main text, or Methods section.

n/a	Confirmed
☐	☒ The exact sample size (*n*) for each experimental group/condition, given as a discrete number and unit of measurement
☐	☒ A statement on whether measurements were taken from distinct samples or whether the same sample was measured repeatedly
☐	☒ The statistical test(s) used AND whether they are one- or two-sided *Only common tests should be described solely by name; describe more complex techniques in the Methods section.*
☒	☐ A description of all covariates tested
☐	☒ A description of any assumptions or corrections, such as tests of normality and adjustment for multiple comparisons
☐	☒ A full description of the statistical parameters including central tendency (e.g. means) or other basic estimates (e.g. regression coefficient) AND variation (e.g. standard deviation) or associated estimates of uncertainty (e.g. confidence intervals)
☐	☒ For null hypothesis testing, the test statistic (e.g. *F*, *t*, *r*) with confidence intervals, effect sizes, degrees of freedom and *P* value noted *Give P values as exact values whenever suitable.*
☒	☐ For Bayesian analysis, information on the choice of priors and Markov chain Monte Carlo settings
☒	☐ For hierarchical and complex designs, identification of the appropriate level for tests and full reporting of outcomes
☒	☐ Estimates of effect sizes (e.g. Cohen's *d*, Pearson's *r*), indicating how they were calculated

Our web collection on statistics for biologists contains articles on many of the points above.

Software and code

Policy information about availability of computer code

Data collection: Applied Biosystems 7500 fast and 7500 Real-Time PCR System (7500 v2.3) was used to collect relative gene expression (RQ) values. Zeiss ZEN (2.3 SP1 FP3 895 black, 64 bit, release version 14.0.0.0) was used to collect confocal images. Flow cytometry data were acquired with BD FACSDIVA™ v8.0.1. Living Image v 4.5 was used to collect luminescence images. NIS-Elements BR 3.0 was used to take bright field images of HE staining. LabSolutions V5.86 SPl was used to collect HPLC/MS data. ZetaVIEW v 8.05.11 SP4 was used to collect data of nanoparticle tracking analysis. ESI SC 2.9.0.202 was used to collect ICP-MS data. OpenVnmrj v2.1 REVISION A was used to collect NMR spectrum data. Sequencing output from the Illumina MiSeq platform were converted to fastq format and demultiplexed using Illumina Bcl2Fastq 2.20.0 (Illumina, Inc. USA). The resulting paired-end reads were processed with the Quantitative Insights Into Microbial Ecology (QIIME) 2 2021-2 wrapper for DADA2 including merging paired ends, quality filtering, error correction, and chimera detection. Living Image® version 4.5 software was used to collect IVIS data. UV absorption for MTT and protein quantifications were collected by Mikrowin 2000. Image Lab 6.0 Software (BIO-RAD) was used to image western blots.

Data analysis	Flow cytometry data were analyzed with FlowJo Vl0. ImageJ v2.10 was used for confocal, TEM and cryoEM images processing. GraphPad Prism 9.0.1 and 9.5.1 was used to plot the data and analyze the statistic differences. The chemical structure were generated by Chemical Draw v14. X calibur v4.1 (ThermoFisher, Breman, Germany) was used to analyze the Mass spectrum data. LabSolutions V5.86 SPl was used to analyze HPLC/MS data. ZetaVIEW analyze v8.05.ll SP4 was used to analyze the data of nanoparticle tracking analysis. Image deconvolution algorithms were done by Autoquant X3.l. Image reconstruction was done by Imaris 9.5.1. Amplicon sequencing units from DADA2 were assigned taxonomic identifiers with respect to the Greengenes and Silva databases, their sequences were aligned using maFFT in QIIME 2, and a phylogenetic tree was built with FastTree in QIIME 2. The linear discriminant analysis effect size (LEfSe) Galaxy module was used for analysis examining biologic consistency and effect relevance, which was conducted by coupling standard tests for statistical significance. FASTQ files of whole exome sequencing were subjected to FASTQC (v0.11.4) to check raw sequencing quality and TrimGalore (v0.6.0) to remove low-quality bases adapters and short reads.

For manuscripts utilizing custom algorithms or software that are central to the research but not yet described in published literature, software must be made available to editors and reviewers. We strongly encourage code deposition in a community repository (e.g. GitHub). See the Nature Portfolio guidelines for submitting code & software for further information.

Data

Policy information about availability of data

All manuscripts must include a data availability statement. This statement should provide the following information, where applicable:

- Accession codes, unique identifiers, or web links for publicly available datasets
- A description of any restrictions on data availability
- For clinical datasets or third party data, please ensure that the statement adheres to our policy

The 16S rRNA data are available through NCBI public repository Sequence Read Archive (accession number: SRR23197060-SRR23197067, BioProject PRJNA926798). The whole exome sequencing data are available through NCBI public repository Sequence Read Archive (accession number: BioProject PRJNA926643). The genome of Fusobacterium nucleatum subsp. nucleatum ATCC 25586 (GCA_000007325.1) is available on KEGG (https://www.genome.jp/kegg-bin/show_organism?org=fnu). Mus musculus genome (GRCm39 reference Annotation Release 109) is available on NCBI (https://www.ncbi.nlm.nih.gov/genome/annotation_euk/Mus_musculus/109/). Fusobacterium nucleatum reference proteome (UP000002521_190304) is available on EBI (https://www.ebi.ac.uk/reference_proteomes/). The distance map for FISH images analysis is available on Zenodo (DOI: 10.5281/zenodo.8200515). All other data supporting the findings of this study are available from the corresponding authors upon reasonable request. Source data are provided with this paper.

Human research participants

Policy information about studies involving human research participants and Sex and Gender in Research.

Reporting on sex and gender	In the clinical cohort of colorectal cancer gender as reported to the Health insurance system is reported and gender is accounted for in the multivariate model as gender was identified as a prognosis factor for 3 year DFS in univariate analyses. For the breast cancer clinical cohort, only female patients as reported to the French health insurance system were included.
Population characteristics	Covariates Used in the Multivariate Model: gender, age (18-49, 50-69, 70-79, ≥ 80 years), laterality of cancer Charlson comorbidity index (none, 1-2, ≥3), nutritional status during the surgical resection (malnutrition vs. no malnutrition), admission to the intensive care unit during the surgical resection length of stay (no admission or <2 days, 2-7 days, >7 days), and time when antibiotics were used along the time axis to account for a potential time-dependent bias.
Recruitment	The clinical study was performed by analyzing the French Cancer Cohort from the cancer institute data platform of the French National Cancer Institute (INCa), the prospective cohort of which is an extraction from the National Health Data System (SNDS) and includes all people diagnosed, treated, or followed up for cancer in France since 2010. In brief, this study included all people aged 18 or older with incident nonmetastatic colorectal cancer resected between January 2012 and December 2014 in France. To select incident cases, we excluded people with a previous history of cancer (2010-2011) or long-term disease for cancer (diagnosed before 2012).
Ethics oversight	The French cancer cohort protocol was approved by a national committee (Comité Consultatif sur le Traitement de l'Information en Matière de Recherche dans le Domaine de la Santé) and authorized by the French Data Protection Agency (Commission nationale de l'informatique et des libertés—Cnil, number 2019-082).

Note that full information on the approval of the study protocol must also be provided in the manuscript.

Field-specific reporting

Please select the one below that is the best fit for your research. If you are not sure, read the appropriate sections before making your selection.

☒ Life sciences ☐ Behavioural & social sciences ☐ Ecological, evolutionary & environmental sciences

For a reference copy of the document with all sections, see nature.com/documents/nr-reporting-summary-flat.pdf

Life sciences study design

All studies must disclose on these points even when the disclosure is negative.

Sample size	Sample size was determined by power analysis (90% power at 5% significance level).
Data exclusions	No exclusion criteria were incorporated in the design of the experiments for this study and no data were excluded from analyses.
Replication	For each series of experiments, all replication attempts were successful. The experiment repeats have been added to each panel.
Randomization	Mice, cells and bacteria for studies were randomly allocated to experimental groups at the beginning of experiments.
Blinding	Samples were labeled with simple numbers before data analysis. The investigators were blinded to group allocation during data collection.

Reporting for specific materials, systems and methods

We require information from authors about some types of materials, experimental systems and methods used in many studies. Here, indicate whether each material, system or method listed is relevant to your study. If you are not sure if a list item applies to your research, read the appropriate section before selecting a response.

Materials & experimental systems

n/a	Involved in the study
☐	☒ Antibodies
☐	☒ Eukaryotic cell lines
☒	☐ Palaeontology and archaeology
☐	☒ Animals and other organisms
☒	☐ Clinical data
☒	☐ Dual use research of concern

Methods

n/a	Involved in the study
☒	☐ ChIP-seq
☐	☒ Flow cytometry
☒	☐ MRI-based neuroimaging

Antibodies

Antibodies used

The antibodies used in this study were summarized in Supplementary Table S2.
MSH2, (Cell Signaling, 50-204-7020) WB dilution 1:1000
MSH6, (Cell Signaling, 50-204-7740) WB dilution1:1000
MLH1, (Abcam, EPR3894) WB dilution 1:2000
CD8 Alexa Fluor® 700 (Biolegend, 155022) Flow cytometry, dilution 1:100
CD3 PE-Cy7 (Biolegend, 100219) Flow cytometry 1:100
CD206 PerCP-Cy5.5 (Biolegend, 141715) Flow cytometry, dilution 1:100
F4/80 PE-Cy5 (Biolegend, 12311) Flow cytometry, dilution 1:100
CD8 PE (BD Pharmingen, 553032) Flow cytometry, dilution 1:100
CD3 Alexa Fluor® 647 (BioLegend, 100209) Flow cytometry, dilution 1:100
CD4 Percy-Cy5.5 (BioLegend, 100434) Flow cytometry, dilution 1:100
CD11b FITC (BioLegend, 101205) Flow cytometry, dilution 1:100
F4/80 Alexa Fluor® 488 (Invitrogen, 15-4801-80) Flow cytometry, dilution 1:100
CD206 PE-Cy7 (eBioscience, 25-2061-80) Flow cytometry, dilution 1:100
CD62L APC (BioLegend, 104411) Flow cytometry, dilution 1:100
CD44 FITC (BioLegend,103006) Flow cytometry, dilution 1:100
INF-γ BV421 (Invitrogen, 48-7311-80) Flow cytometry, dilution 1:100
CD31 Alexa Fluor® 647 (BioLegend, 102516) IF, dilution 1:200
LYVE-1 Alexa Fluor® 488 (Invitrogen, 53-0443-82) IF, dilution 1:500
HIF-1 (Invitrogen, PA5-85494) IF, dilution1:1000
Anti-Rabbit IgG Alexa Fluor® 594 (Abcam, AB150077) IF, dilution 1:1000
CD206 PE (BioLegend, 141705) IF, dilution 1:500
CD8 FITC (BioLegend, 100705) IF, dilution 1:500
CD11c Percy-CY5.5 (BioLegend, 117327) Flow cytometry, dilution 1:100
MHCII PE-CY7 (BioLegend, 107629) Flow cytometry, dilution 1:100
Gr-1 Alexa Fluor® 594 (BioLegend, 108448) Flow cytometry, dilution 1:100
Anti-CD8 (Bioxcell, BP0004-1) i.v. injection
Anti-CD4 (Biocell, BE0003-1) i.v. injection
IgG (Bioxcell, BE0094) i.v. injection
Calriticulin (Abcam, AB2907) Western blot and IF, WB dilution 1:1000, IF dilution 1:100
Heat shock protein 70 (Invitrogen, MA5-31961) Western blot dilution 1:3000
Beta-actin (Invitrogen, MA5-32479) Western blot, dilution 1:1000
Anti-Rabbit IgG HRP (Invitrogen, 31460) Western blot, dilution 1:10000

Validation

All antibodies were verified by the supplier and each lot has been quality tested. All the antibodies used are from commercial sources and have been validated by the vendors. Validation data are available on the manufacturer's website.

CD8 Alexa Fluor® 700 (Biolegend 155022) has been validated to be used for flow cytometric analysis and mentioned species reactivity with mouse. https://www.biolegend.com/de-at/cell-health/pe-cyanine7-anti-mouse-cd8a-antibody-1906

MSH2, (Cell Signaling, 50-204-7020) has been validated to be used for western blot and mentioned species reactivity with mouse. https://www.cellsignal.com/products/primary-antibodies/msh2-d24b5-xp-rabbit-mab/2017?_requestid=624578

MSH6, (Cell Signaling, 50-204-7740) has been validated to be used for western blot and mentioned species reactivity with mouse. https://www.cellsignal.com/products/primary-antibodies/msh6-p150-antibody/3995

MLH1, (Abcam, EPR3894) has been validated to be used for western blot and mentioned species reactivity with mouse. https://www.abcam.com/products/primary-antibodies/mlh1-antibody-epr3894-ab92312

CD206 PerCP-Cy5.5 (Biolegend, 141715) has been validated to be used for flow cytometric analysis and mentioned species reactivity with mouse. https://www.biolegend.com/fr-fr/products/percp-cyanine5-5-anti-mouse-cd206-mmr-antibody-8477

F4/80 PE-Cy5 (Biolegend, 12311) has been validated to be used for flow cytometric analysis and mentioned species reactivity with mouse. https://www.biolegend.com/de-de/products/pe-cyanine5-anti-mouse-f4-80-antibody-4069

CD3 PE-Cy7 (Biolegend, 100219) has been validated to be used for flow cytometric analysis and mentioned species reactivity with mouse. https://www.biolegend.com/ja-jp/clone-search/pe-cyanine7-anti-mouse-cd3-antibody-6060

CD8 PE (BD Pharmingen, 553032) has been validated to be used for flow cytometric analysis and mentioned species reactivity with mouse. https://www.bdbiosciences.com/en-us/products/reagents/flow-cytometry-reagents/research-reagents/single-color-antibodies-ruo/pe-rat-anti-mouse-cd8a.553032

CD3 Alexa Fluor® 647 (BioLegend, 100209) has been validated to be used for flow cytometric analysis and immunofluorescence and mentioned species reactivity with mouse. https://www.biolegend.com/en-us/products/alexa-fluor-647-anti-mouse-cd3-antibody-2693

CD4 Percy-Cy5.5 (BioLegend, 100434) has been validated to be used for flow cytometric analysis and mentioned species reactivity with mouse. https://www.biolegend.com/fr-ch/products/percp-cyanine5-5-anti-mouse-cd4-antibody-4220?GroupID=BLG4745

CD11b FITC (BioLegend, 101205) has been validated to be used for flow cytometric analysis and mentioned species reactivity with mouse. https://www.biolegend.com/en-us/cellular-dyes-and-ancillary-products/fitc-anti-mouse-human-cd11b-antibody-347

F4/80 Alexa Fluor® 488 (Invitrogen, 15-4801-80) has been validated to be used for flow cytometric analysis and mentioned species reactivity with mouse. https://www.thermofisher.com/antibody/product/F4-80-Antibody-clone-BM8-Monoclonal/53-4801-82

CD206 PE-Cy7 (eBioscience, 25-2061-80) has been validated to be used for flow cytometric analysis and mentioned species reactivity with mouse. https://www.thermofisher.com/antibody/product/CD206-MMR-Antibody-clone-MR6F3-Monoclonal/25-2061-82

CD62L APC (BioLegend, 104411) has been validated to be used for flow cytometric analysis and mentioned species reactivity with mouse. https://www.biolegend.com/en-ie/cell-health/apc-anti-mouse-cd62l-antibody-381

CD44 FITC (BioLegend, 103006) has been validated to be used for flow cytometric analysis and mentioned species reactivity with mouse. https://www.biolegend.com/fr-fr/sean-tuckers-tests/fitc-anti-mouse-human-cd44-antibody-314?GroupID=BLG10248

INF-γ BV421 (Invitrogen, 48-7311-80) has been validated to be used for flow cytometric analysis and mentioned species reactivity with mouse. https://www.thermofisher.com/antibody/product/IFN-gamma-Antibody-clone-XMG1-2-Monoclonal/48-7311-82

HIF-1 N/A (Invitrogen, PA5-85494) has been validated to be used for western blot and immunofluorescence and mentioned species reactivity with mouse. https://www.thermofisher.com/antibody/product/HIF1A-Antibody-Polyclonal/PA5-85494

Anti-Rabbit IgG Alexa Fluor® 594 (Abcam, AB150077) has been validated to be used for immunofluorescence and mentioned species reactivity with rabbit. https://www.abcam.com/products/secondary-antibodies/goat-rabbit-igg-hl-alexa-fluor-594-ab150080.html

CD206 PE (BioLegend, 141705) has been validated to be used for flow cytometric analysis and mentioned species reactivity with mouse https://www.biolegend.com/de-de/sean-tuckers-tests/pe-anti-mouse-cd206-mmr-antibody-7424?GroupID=BLG9506

CD8 FITC (BioLegend, 100705) has been validated to be used for flow cytometric analysis and mentioned species reactivity with mouse. https://www.biolegend.com/en-us/products/pe-anti-mouse-ccl5-rantes-antibody-10420?GroupID=BLG13391

CD11c Percy-CY5.5 (BioLegend, 117327) has been validated to be used for flow cytometric analysis and mentioned species reactivity with mouse. https://www.bdbiosciences.com/en-us/products/reagents/flow-cytometry-reagents/research-reagents/single-color-antibodies-ruo/percp-cy-5-5-hamster-anti-mouse-cd11c.560584#:~:text=CD11c%20plays%20a%20role%20in%20binding%20of%20iC3b.&text=PerCP%2DCy5.5-,PerCP%2DCy5.,Em%20Max)%20at%20676%20nm.

MHCII PE-CY7 (BioLegend, 107629) has been validated to be used for flow cytometric analysis mentioned species reactivity with mouse. https://www.biolegend.com/de-de/explore-new-products/pe-cyanine7-anti-mouse-i-a-i-e-antibody-6136?GroupID=BLG11931

Gr-1 Alexa Fluor® 594 (BioLegend, 108448) has been validated to be used for immunofluorescence and flow cytometric analysis and

mentioned species reactivity with mouse. https://www.biolegend.com/de-de/products/alexa-fluor-594-anti-mouse-ly-6g-ly-6c-gr-1-antibody-9672

Anti-CD8 (Bioxcell, BP0004-1) has been validated to be used for western blot and mentioned species reactivity with mouse. https://bioxcell.com/invivomab-anti-mouse-cd8a-be0004-1

Anti-CD4 (Bioxcell, BE0003-1) has been validated to be used for western blot and mentioned species reactivity with mouse. https://bioxcell.com/invivomab-anti-mouse-cd4-be0003-1

IgG (Biocell, BE0094) It has been described as ideal for use as a non-reactive control IgG. https://bioxcell.com/invivomab-polyclonal-rat-igg-be0094

Calriticulin (Abcam, AB2907) has been validated to be used for immunofluorescence and western blot and mentioned species reactivity with mouse. https://www.abcam.com/products/primary-antibodies/calreticulin-antibody-er-marker-ab2907.html

Heat shock protein 70 (Invitrogen, MA5-31961) has been validated to be used for western blot, immunofluorescence and flow cytometric analysis and mentioned species reactivity with mouse. https://www.thermofisher.com/antibody/product/HSP70-Antibody-clone-SA0379-Recombinant-Monoclonal/MA5-31961

Beta-actin (Invitrogen, MA5-32479) has been validated to be used for western blot, immunofluorescence and flow cytometric analysis and mentioned species reactivity with mouse. https://www.thermofisher.com/antibody/product/Actin-Antibody-clone-JJ09-29-Recombinant-Monoclonal/MA5-32479

Anti-Rabbit IgG HRP (Invitrogen, 31460) has been validated to be used for western blot and mentioned species reactivity with mousehttps://www.thermofisher.com/antibody/product/Goat-anti-Rabbit-IgG-H-L-Secondary-Antibody-Polyclonal/31460

Eukaryotic cell lines

Policy information about cell lines and Sex and Gender in Research

Cell line source(s)	Metastatic CT26FL3 cells were kindly provided by Dr. Maria Marjorette O. Peña at the University of South Carolina. CT26FL3(Luc/RFP) cells stably expressing red fluorescent protein (RFP) and luciferase (Luc) were established by transfection with lentivirus vectors carrying RFP and Luc genes and a puromycin resistance gene. MC38 cells were purchased from Kerafast, Inc..
Authentication	None of the cell lines used were authenticated.
Mycoplasma contamination	The cell lines were tested negative for mycoplasma contamination .
Commonly misidentified lines (See ICLAC register)	No cell lines used are listed in the database of commonly misidentified cell lines.

Animals and other research organisms

Policy information about studies involving animals; ARRIVE guidelines recommended for reporting animal research, and Sex and Gender in Research

Laboratory animals	Animals were maintained in a specific pathogen-free facility (12-hour light/dark cycle, tempeature: 21-23 °C, humidity: 30-70%). All mice were used at 6-8 weeks of age, age and sex matched for the experiment.
Wild animals	The study did not involve wild animals.
Reporting on sex	Balb/CJ and C57BL/6J mice were female. Sex were not considered in study design.
Field-collected samples	The study did not involve samples collected from the filed.
Ethics oversight	All animal handling protocols were approved by the University of North Carolina at Chapel Hill's Institutional Animal Care and Use Committee.

Note that full information on the approval of the study protocol must also be provided in the manuscript.

Flow Cytometry

Plots

Confirm that:

☒ The axis labels state the marker and fluorochrome used (e.g. CD4-FITC).

☒ The axis scales are clearly visible. Include numbers along axes only for bottom left plot of group (a 'group' is an analysis of identical markers).

☒ All plots are contour plots with outliers or pseudocolor plots.

☒ A numerical value for number of cells or percentage (with statistics) is provided.

Methodology

Sample preparation	Freshly harvested tumor tissues were digested into single cell suspensions in PBS with collagenase II (200 U/ml, Invitrogen) and DNase (100 μg/mL, Invitrogen) at 37 °C for 60 min. Single cell suspension was collected by mechanical disruption using the plunger end of a 1 mL syringe, and diluted to 1×106 cells/mL with FACS buffer (PBS containing 2% bovine calf serum and 2 mM EDTA). One milliliter of the cell suspension was centrifuged and stained at 4 °C for 30 min by the addition of a cocktail of fluorophore conjugated antibodies (Supplementary Table 2). For intracellular staining, cells were permeabilized with Cytofix/Cytoperm buffer (BD Biosciences), and then stained with intracellular antibodies at 4 °C for 20 min. Cells were fixed with 4% PFA and analyzed by flow cytometry.
Instrument	BD LSR II, LSRFortessa
Software	FACSDIVA™ v8.0.1
Cell population abundance	All cells are used for analysis of a relevant cell population. Cell count of at least 25,000 events was collected of a relevant cell population after the initial gating.
Gating strategy	Preliminary cell populations were gated for singlets using FSC-A/SSC-A. Control stains were used to distinguish between background staining and specific antibody staining. Specific immune cell populations were gated based on the specific antibody staining as described in each experiment.

☒ Tick this box to confirm that a figure exemplifying the gating strategy is provided in the Supplementary Information.